

1 **Multiple Optimal Depth Predictors Analysis (MODPA) for River Bathymetry:**  
2 **Findings from Spectroradiometry, Simulations, and Satellite Imagery**

3 Milad Niroumand-Jadidi<sup>\*a, b, c</sup>, Alfonso Vitti<sup>a</sup> and David R. Lyzenga<sup>d</sup>

4  
5 <sup>a</sup> *Department of Civil, Environmental, and Mechanical Engineering, University of Trento, Via Mesiano,*  
6 *77 - 38123 Trento, Italy. Email: m.niroumand@unitn.it*

7 <sup>b</sup> *Department of Biology, Chemistry, and Pharmacy, Freie Universität Berlin, Altensteinstraße 6, 14195*  
8 *Berlin, Germany.*

9 <sup>c</sup> *Leibniz-Institute of Freshwater Ecology and Inland Fisheries, Müggelseedamm 310, 12587 Berlin,*  
10 *Germany*

11 <sup>d</sup> *Department of Naval Architecture and Marine Engineering, College of Engineering, University of*  
12 *Michigan, 115 NAME Bldg., 2600 Draper Dr. Ann Arbor, MI 48109-2145, Michigan, USA.*  
13

14 **Abstract:**

15 Remote mapping of bathymetry can play a key role in gaining spatial and temporal insight into fluvial  
16 processes, ranging from hydraulics and morphodynamics to habitat conditions. This research introduces  
17 Multiple Optimal Depth Predictors Analysis (MODPA), which combines previously developed depth  
18 predictors along with additional predictors derived from the intensity component of the HSI color space  
19 transformation. MODPA empirically selects a set of optimal predictors among all candidates utilizing  
20 partial least squares (PLS), stepwise, or principal component (PC) regression models. The primary focus of  
21 this study was on shallow (< 1 m deep) and clearly flowing streams where substrate variability could have  
22 a pronounced effect on depth retrieval. Spectroscopic experiments were performed under controlled  
23 conditions in a hydraulic laboratory to examine the robustness of bathymetry models with respect to  
24 changes in bottom type. Further, simulations from radiative transfer modeling were used to extend the  
25 analysis by isolating the effect of inherent optical properties (IOPs) and by investigating the performance  
26 of bathymetry models in optically complex and deeper streams. The bathymetry of the Sarca River, a  
27 shallow river in the Italian Alps, was mapped using a WorldView-2 (WV-2) image, for which we evaluated  
28 the atmospheric compensation (AComp) product. Results indicated the greater robustness of multiple-  
29 predictor models particularly MODPA rather than single-predictor models, such as Optimal Band Ratio

30 Analysis (OBRA), with respect to heterogeneity of bottom types, IOPs, and atmospheric effects. The HSI  
31 intensity component enhanced the accuracy of depth retrieval, particularly in optically-complex waters and  
32 also for low spectral resolution imagery (e.g., GeoEye). Further, the enhanced spectral resolution of WV-2  
33 imagery improved bathymetry retrieval compared to 4-band GeoEye data.

34 **Keywords:** bathymetry, river, Lyzenga model, ratio model, depth predictors, spectroscopy, WorldView-2,  
35 atmospheric compensation (AComp)

## 36 **1- Introduction**

37 Remote sensing techniques provide an alternative to traditional field-based measurements and have the  
38 potential to enhance our understanding of fluvial systems by providing spatially and temporally explicit  
39 information (Marcus and Fonstad, 2008; Carbonneau et al., 2012; Legleiter and Overstreet, 2012;  
40 Niroumand-Jadidi and Vitti, 2016; Shintani and Fonstad, 2017; Niroumand-Jadidi and Vitti, 2017a). The  
41 recent integration of remote sensing and river sciences has emerged as a growing research field termed  
42 “fluvial remote sensing” (Marcus and Fonstad, 2010; Carbonneau et al., 2012). Advancements in sensors,  
43 such as water-penetrating, green-wavelength light detection and ranging (LiDAR), or platforms, such as  
44 unmanned aerial vehicles (UAVs), have recently provided new tools for characterizing fluvial systems  
45 (Kinzel et al., 2013; Flener et al., 2013; Shintani and Fonstad, 2017). However, green LiDAR observations  
46 are mainly feasible by means of low-altitude platforms (e.g., manned aircrafts), which leads to a lower  
47 spatial and temporal coverage compared to optical sensing by means of satellites. Furthermore, the  
48 application of green LiDAR in riverine environments is hindered by low point density of observations and  
49 also the confusion among laser returns from the water surface, water column, and riverbed (Legleiter and  
50 Overstreet, 2012; Kinzel et al., 2013). UAVs offer the potential for higher spatial and temporal resolution,  
51 but at the cost of spatial coverage. In this context, passive optical remote sensing aboard airborne and  
52 spaceborne platforms remains a broadly applicable means of characterizing a wide range of attributes in  
53 fluvial systems, including bathymetry (Legleiter and Overstreet, 2012; Niroumand-Jadidi and Vitti, 2016),

54 substrate type and composition (Legleiter et al., 2016), grain size (Carbonneau et al., 2004; Niroumand-  
55 Jadidi and Vitti, 2017b), and hydromorphological units (Legleiter et al., 2004).

56 Bathymetry is one of the key applications of remote sensing to fluvial systems that facilitates understanding  
57 river form, process, and function (Shintani and Fonstad, 2017). Information on water depth can play a  
58 valuable role in mapping in-stream habitats (Carbonneau et al., 2012; Hugue et al., 2016), parameterization  
59 and analysis of hydro-morphological processes (Bryant and Gilvear, 1999; Flener et al., 2012), and river  
60 management (Fonstad and Marcus, 2005; Legleiter and Overstreet, 2012). Optical sensors onboard aerial  
61 and satellite platforms have long been used for studying shallow coastal environments (Lyzenga, 1978;  
62 Lyzenga, 1981, Philpot, 1989; Dierssen et al., 2003; Louchard et al., 2003; Lesser and Mobley, 2007).  
63 Because of their smaller spatial scales, fluvial systems have mostly utilized aerial imagery to derive  
64 bathymetric data (Winterbottom and Gilvear, 1997; Jordan and Fonstad, 2005; Walther et al., 2011;  
65 Legleiter, 2013). With recent enhancements in spatial resolution of satellite imagery, mapping river  
66 bathymetry from space is receiving more interest due to larger spatial coverage and higher temporal  
67 resolution of satellite sensors than those onboard aerial platforms. Legleiter and Overstreet (2012)  
68 performed a feasibility assessment of mapping the bathymetry of gravel-bed rivers from space using  
69 WorldView-2 (WV-2) imagery.

70 The theoretical basis for optical remote sensing of bathymetry in riverine environments is built upon  
71 research conducted in optically shallow coastal environments (Legleiter et al., 2004; Legleiter et al., 2009).  
72 Bathymetric techniques fall into two main approaches: through-water photogrammetry (Fryer, 1983;  
73 Westaway et al., 2001) and spectrally based analysis (Lyzenga, 1978; Lee et al., 1998). Through-water  
74 photogrammetry utilizes stereo imagery to produce a digital elevation model by accounting for refraction  
75 of light at the air-water interface (Westaway et al., 2001; Lane et al., 2010). One particular type of  
76 photogrammetric approach known as Structure from Motion (SfM) has received growing interest for  
77 measuring bathymetry and characterizing riverbed topography (Woodget et al., 2015; Dietrich, 2017). SfM  
78 is capable of reconstructing three-dimensional geometry using multiple overlapping images taken from a

79 wide range of angles (Shintani and Fonstad, 2017). Spectrally based approaches to deriving bathymetric  
80 data can be divided into physics-based and empirical models (Brando et al., 2009; Dekker et al., 2011). The  
81 first rely on inversion of radiative transfer models and account for the physics of how light interacts with  
82 the water surface, water-column, and bottom (Lee et al., 1998; Lee et al., 1999; Lesser and Mobley, 2007;  
83 Brando et al., 2009), while the latter provide regression-based predictions of bathymetry (Lyzenga, 1978;  
84 Philpot, 1989).

85 The seminal work of Lyzenga (1978, 1981) provides a basis for empirical retrieval of water depths from  
86 optical imagery, which was the focus of this research. Lyzenga's model assumes a linear relation between  
87 an image-derived quantity ( $X$ ) and the water depth ( $d$ ), where  $X$  is a predictor obtained from log-  
88 transformation of image values in a given spectral band. Multiple regression (Lyzenga, 1985; Lyzenga et  
89 al., 2006) and ratio methods (Stumpf et al., 2003) have been demonstrated to enhance the robustness of  
90 bathymetry retrieval with respect to substrate variability and water quality heterogeneity. The first employs  
91 multiple spectral bands to perform a multiple linear regression between image-derived predictors ( $X$ ) and  
92 water depths ( $d$ ) while the latter model considers a log-transformed band ratio as a single predictor of water  
93 depth. More recently, Optimal Band Ratio Analysis (OBRA) was introduced to identify the pair of bands,  
94 among all possible pairs, for which the ratio model yields the strongest correlation with water depth  
95 (Legleiter et al., 2009). Each of these types of predictors has been reported as optimal in different case  
96 studies (Legleiter et al., 2012; Bramante et al., 2013; Jawak and Luis, 2016).

97 Further development of new techniques is required to systematically select and combine a set of predictors  
98 that provide robust retrievals in the presence of all the complicating factors that might impact depth retrieval  
99 (e.g., variations in bottom types, IOPs and water-surface roughness). We pursued five main objectives in  
100 this study:

101 (1) Developing a new approach called Multiple Optimal Depth Predictors Analysis (MODPA) for  
102 bathymetry retrieval. This method seeks to identify and incorporate optimal depth predictors among all the  
103 possible Lyzenga and ratio predictors as well as additional predictors from color space transformation. The

104 selection of optimal predictors was performed using several feature selection methods including stepwise,  
105 partial least square (PLS), and principal component (PC) regressions;

106 (2) Assessing the robustness of the proposed MODPA compared to existing models with respect to  
107 heterogeneity in substrate types, IOPs, and atmospheric effects. Bathymetry models were comprehensively  
108 examined using spectroscopic experiments, radiative transfer simulations, and WV-2 imagery. The  
109 spectroscopic experiments were conducted under controlled conditions in a hydraulic laboratory and  
110 involved collecting a set of spectra in a range of water depths with variable substrates. The effects of IOPs,  
111 as influenced by chlorophyll-a (Chl-a), suspended sediment concentration (SSC), and colored dissolved  
112 organic matter (CDOM), were isolated using the simulated data. Moreover, we considered an optically  
113 complex testing scenario where bottom type and IOPs were both allowed to vary;

114 (3) Examining the performance of the proposed MODPA method for bathymetry mapping of the  
115 Sarca River, a shallow and narrow alpine river in Italy, using WV-2 imagery. This analysis quantified the  
116 effectiveness of MODPA compared to other models in the spectrally complex environment of a real case  
117 study. Different strategies were considered for the validation of results including an approach built upon  
118 comparison of image-derived depths with the estimates based on principles of river hydraulics;

119 (4) Assessing the effect of atmospheric correction on bathymetry retrieval of the Sarca River, which  
120 is an important consideration due to the low reflectivity of water bodies and accordingly sizable contribution  
121 of the atmosphere to the total at sensor radiance (Gitelson and Kondratyev, 1991; Mouw et al., 2015). The  
122 newly released surface reflectance product of DigitalGlobe (2016), called atmospheric compensation  
123 (AComp), was assessed to understand the robustness of bathymetric models with respect to atmospheric  
124 effects;

125 (5) Assessing the efficacy of WV-2 sensor's additional spectral bands compared to traditional high  
126 resolution satellite imagery (HRSI, less than 5 m pixel size) with only four bands such as GeoEye.

## 127 **2- Bathymetry from Optical Imagery**

128 In the context of optical remote sensing of water bodies, the total radiance reaching the sensor at a given  
129 wavelength  $\lambda$ ,  $L_T(\lambda)$ , consists of four main components: upwelling radiances from the bottom,  $L_b(\lambda)$ , water  
130 column,  $L_c(\lambda)$ , and surface of the water body,  $L_s(\lambda)$ , as well as the atmospheric path radiance,  $L_p(\lambda)$ . These  
131 components are summarized in the following equation (Legleiter et al., 2004; Legleiter et al., 2009):

$$132 \quad L_T(\lambda) = L_b(\lambda) + L_c(\lambda) + L_s(\lambda) + L_p(\lambda) \quad (1)$$

133 Aside from  $L_p(\lambda)$ , each of these radiance components can be associated with a specific property of the  
134 water body. For instance, the surface-reflected component of the radiance can be linked to the roughness  
135 of the water surface, which in turn is a function of local hydraulics in riverine environments and can  
136 potentially reveal information about flow velocity (Overstreet and Legleiter, 2017; Legleiter et al., 2017).  
137 Information on bathymetry is embedded in the bottom-reflected radiance component, which is affected not  
138 only by water depth but also by bottom type and indirectly by water column optical properties (Lee et al.,  
139 1998; Stumpf et al., 2003; Legleiter et al., 2009). Thus, it is essential to isolate the radiance component of  
140 interest or to reduce the effect of other extraneous components in order to retrieve the desired parameter,  
141 which in this study is the water depth.

142 Lyzenga's model (1978, 1981) is built upon the Beer-Lambert law, which describes the exponential  
143 attenuation of light travelling through the water column. This model includes a deep-water correction  
144 term,  $L_w(\lambda)$ , equated with the radiance observed over optically-deep water, to account for the radiance  
145 scattered from the water column, water surface, and atmosphere (Eq. 2).

$$146 \quad L_w(\lambda) = L_c(\lambda) + L_s(\lambda) + L_p(\lambda) \quad (2)$$

147 The bottom-reflected radiance can be considered negligible for optically-deep waters. Therefore,  
148 subtracting  $L_w(\lambda)$  from all water pixels leaves the bottom-reflected radiance, which contains bathymetry  
149 information. According to Lyzenga's model, the water depth ( $d$ ) depends linearly on the predictor ( $X$ )  
150 derived from image values in a given spectral band (Eqs. 3 and 4).

151

152  $X = \ln(L_T(\lambda) - L_w(\lambda))$  (3)

153  $d = aX + b$  (4)

154 Note that deep-water correction required for Lyzenga's model has been demonstrated to be  
155 negligible for shallow rivers (Mumby and Edwards, 2000; Flener et al., 2012; Flener, 2013). This is mainly  
156 because the bottom signal is the dominant component of radiance reaching the sensor, particularly if the  
157 image has been atmospherically corrected. Therefore, there is low probability to approach to the deep-water  
158 signal in shallow and clear rivers (Legleiter et al., 2009). Note that type of the substrate is also an important  
159 factor influencing the total water-leaving radiance. For instance, depth retrieval in very shallow waters  
160 could be hindered by the presence of a dark, low-reflectance substrate that absorbs most of the downwelling  
161 radiance. However, this would be a rare case where the bottom-reflected radiance is not sufficient to  
162 propagate through the thin water column in riverine environments. The unknown parameters ( $a$ ,  $b$ ) can be  
163 estimated by means of a simple regression between  $X$  and in-situ depths ( $d$ ). However, these parameters  
164 depend on the IOPs of the water column and the bottom reflectance, which might vary within a given scene.  
165 To deal with these problems, a linear combination of the predictors ( $X_i$ ) derived from multiple ( $n$ ) spectral  
166 bands (Eq. 5) has been suggested for depth estimation (Lyzenga et al., 2006).

167  $d = \sum_{i=1}^n a_i X_i + b$  (5)

168 Note that water-surface roughness and accordingly surface-reflected radiance can also vary  
169 significantly within a given river channel on small spatial scales (Legleiter et al., 2009). These effects cause  
170 variations in near-infrared bands, which do not contain significant bottom-reflected signals because of  
171 strong attenuation of near-infrared light. Thus, scaled versions of the near-infrared bands can be  
172 instrumental for enhancing the robustness of depth retrieval with respect to variations in water surface  
173 roughness, as well as atmospheric effects (Lyzenga et al., 2006; Kay et al., 2009).

174 Stumpf et al. (2003) proposed using a ratio model for depth retrieval to mitigate the undesirable  
175 effect of variations in bottom reflectance (Eq. 6).

176 
$$X = \ln \left[ \frac{L_T(\lambda_1)}{L_T(\lambda_2)} \right] \quad (6)$$

177 The ratio model relies on the fact that different substrates at the same depth have approximately  
178 equal values of the ratio between total radiances at two different wavelengths. Such a ratio can be used as  
179 a robust depth predictor with respect to substrate variability (Stumpf et al., 2003; Flener, 2013). Note that  
180 Equation 6 is a special case of Equation 5, with  $n = 2$  and  $a_2 = -a_1$ . So this method is similar to that of  
181 Lyzenga, but does not involve deep-water correction. Legleiter et al. (2009) extended the idea of the ratio  
182 model in the form of OBRA. This model examines all the possible pairs of bands to identify the pair that  
183 provides the highest coefficient of determination ( $R^2$ ) in a regression of  $X$  against  $d$ .

184 Bathymetric models originally developed for coastal environments have only recently been translated to  
185 fluvial systems, particularly using HRSI (Legleiter and Overstreet, 2012). The key distinction between  
186 coastal and riverine environments is the thinner water-column in rivers. Therefore, a relatively high  
187 contribution from the river substrate and a relatively low contribution from the water column can be  
188 expected, especially in shallow and clearly flowing streams. Although this is advantageous for depth  
189 retrieval due to having stronger bottom-reflected radiance, the pronounced effect of substrate variability  
190 complicates depth retrieval. Moreover, as mentioned before, highly variable water-surface roughness in  
191 fluvial systems can induce additional challenges. Therefore, development of robust methods is needed to  
192 produce reliable and consistent bathymetric maps for large spatial extents using optical imagery.

### 193 **3- Multiple Optimal Depth Predictors Analysis (MODPA)**

194 Existing bathymetric models employ one or more Lyzenga predictors or a single ratio predictor. Although  
195 OBRA identifies the optimal ratio predictor, the model is based on a sole ratio predictor. The selection  
196 between predictor types (Lyzenga or ratio) can be challenging in practice, as the results of previous studies  
197 indicated that each type of predictor can possibly lead to more accurate results than the other, depending  
198 on the case study. For instance, Jawak and Luis (2016) reported that the Lyzenga model derived the  
199 bathymetry of a shallow lake (depth < 8 m) more precisely (with 15% higher  $R^2$  and 0.98 m lower RMSE)  
200 than the ratio model using WV-2 imagery. Bathymetry models that rely on a simple regression (e.g., OBRA)



201 attempt to explain the dependent variable (i.e., depth) using only one predictor; other informative predictors  
202 might be neglected.

203 This research aimed to integrate previously developed depth predictors by initially considering all of the  
204 possible Lyzenga and ratio predictors rather than relying upon only one of the predictor types. In addition,  
205 we considered some additional predictors derived from the RGB to HSI (hue, saturation, intensity) color  
206 space transformation. More specifically, the intensity component of the HSI space (hereafter called  
207 intensity) was added to the original image feature space and included as a potential predictor along with the  
208 associated Lyzenga and ratio predictors. The intensity (I) component refers to the total brightness or  
209 luminance of the pixels, which is associated with the human perception of brightness (Carper et al., 1990).  
210 The intensity component would potentially contribute to depth retrieval because the overall brightness of  
211 image pixels is influenced by the optical properties of the water body (Stumpf et al., 2003), which provides  
212 a physical basis for considering intensity components as candidate depth predictors. However, as a general  
213 rule in regression analysis, new features created through transformation of the original spectral data can  
214 provide a better discriminative ability but might not have a clear physical meaning (Markovitch and  
215 Rosenstein, 2002; Qian et al., 2012). Note that the color space transformation can be applied to each  
216 combination of three spectral bands so that several intensity bands can be added to the feature space (e.g.,  
217 four intensity bands can be derived for a 4-band GeoEye image). A multiple regression approach was then  
218 considered to retain and exploit most of the variability of the predictors. However, making use of all the  
219 predictors can pose the problem of overfitting (Howley et al., 2006). Furthermore, high dimensional  
220 predictors can invite redundant or correlated predictors which can lead to degradation of regression model's  
221 prediction accuracy (Reunanen, 2003; Howley et al., 2006). For example, 36 initial predictors can be  
222 derived from 8-band WV-2 imagery (8 Lyzenga predictors and 28 ratio predictors), and this number will  
223 increase by intensity predictors. Therefore, performing a dimensionality reduction on all the candidate  
224 predictors is essential. This study attempted to select the optimal predictors by using three different

225 regression methods: partial least squares (PLS), stepwise, and principal components (PC). The resultant  
226 optimal predictors can then be a combination of Lyzenga, ratio, and intensity predictors.

227 Stepwise regression is a systematic method for adding and removing terms (predictors) from a linear model  
228 based on their statistical significance in explaining the response variable. Stepwise regression uses the  $p$ -  
229 value of an  $F$ -statistic to test models with and without a potential term at each step. PC and PLS are both  
230 regression methods that construct new predictors called components as linear combinations of the original  
231 predictors. A subset of components then can be selected as optimal predictors in such a way as to keep most  
232 of the variability of the original predictors. The number of components can be chosen by looking at the  
233 percent of variance explained in the response variable as a function of the number of components. However,  
234 PC creates the components without considering the response variable (i.e., depth) while PLS takes the  
235 response variable into account (Haenlein and Kaplan, 2004; Matlab, 2018). The PLS regression optimizes  
236 the prediction power of the model by simultaneous implementation of dimensionality reduction and  
237 regression (Haaland and Thomas, 1988). This means that PLS minimizes the dimensionality of the data  
238 while maximizing the covariance between predictor and response variables. A detailed description of the  
239 PLS regression is given by Wold et al. (2001). These methods provide powerful modeling tools to deal with  
240 large number of predictors when the collinearity among the variables is strong (Abdi, 2003; Li et al., 2014).

#### 241 **4- Hydraulically Assisted Assessment of Bathymetry (HAAB)**

242 In previous studies, bathymetry models were assessed mainly by reserving samples selected at random from  
243 in-situ or simulation data (Legleiter et al., 2004; Legleiter et al., 2009). However, the number of field  
244 measured samples might not be sufficient for both calibration and validation of models. Moreover,  
245 assessment of the depth estimates would not be feasible in reaches not covered during the field survey. In  
246 this study, along with the traditional assessment method, we have used an additional approach, which  
247 integrates some basics of river hydraulics to estimate independent water depths for accuracy assessment.  
248 Fonstad and Marcus (2005) introduced hydraulically assisted bathymetry (HAB), which determines cross-  
249 sectional depths based on principles of open channel flow in order to calibrate the bathymetry model in the

250 absence of in-situ data. We have used the same model but for the assessment of depth estimates, which is  
251 termed, hereafter, as hydraulically assisted assessment of bathymetry (HAAB).

252 The basic formula of discharge (Eq. 7) and the flow resistance equation of Manning (Eq. 8) form the basis  
253 of the HAB model (Fonstad and Marcus, 2005).

$$254 \quad Q = W\bar{d}\bar{V} \quad (7)$$

$$255 \quad \bar{V} = R^{2/3}S^{1/2}/n \quad (8)$$

256 where  $Q$  is the discharge of river.  $\bar{d}$  and  $\bar{V}$  denote average cross-sectional depth and velocity, respectively.  
257  $W$  stands for the width of the cross-section.  $R$  is the hydraulic radius equivalent to the average depth of  
258 cross-section ( $\bar{d}$ ).  $S$  represents the average energy gradient (channel slope), which can be extracted from  
259 digital elevation model or contour maps (Fonstad and Marcus, 2005).  $n$  is hydraulic resistance, which can  
260 be determined for mountain streams according to the following equation (Jarrett, 1984; Fonstad and  
261 Marcus, 2005):

$$262 \quad n = 0.32S^{0.38}R^{-0.16} \quad (9)$$

263 By combining Eqs. 7, 8, and 9,  $\bar{d}$  can be estimated for a given cross-section based on the river discharge  
264 ( $Q$ ), width measurement from image, and slope measurements from topographic maps/data:

$$265 \quad \bar{d} = (Q/3.12WS^{0.12})^{0.55} \quad (10)$$

266 In addition, HAB model approximates the maximum depth of each cross-section ( $d_{max}$ ) based on Robison  
267 and Beschta's (1989) assumption:

$$268 \quad d_{max} = 2\bar{d} \quad (11)$$

269 We have estimated  $\bar{d}$  and  $d_{max}$  for a number of cross-sections along the Sarca River in order to assess the  
270 depth estimates from the proposed MODPA compared to other techniques. The HAAB provided an  
271 additional means of accuracy assessment, which allowed us to assess the bathymetry methods ubiquitously  
272 along the channel and independent from in-situ depths. Note that  $Q$  is the only field information required  
273 for this assessment approach, which was available from the gaging station in the study area.

274 **5- Datasets**

275 The effectiveness of MODPA compared to the Lyzenga model and OBRA was examined by performing a  
 276 wide range of analyses on three independent datasets: (1) Spectroscopic experiments were performed at a  
 277 hydraulic laboratory to acquire measurements of water depth and reflectance under controlled conditions.  
 278 As substrate variability would be the key challenge for bathymetry retrieval in shallow and clearly flowing  
 279 streams, robustness of the models was examined through experiments with two different bottom types  
 280 (Section 5-1); (2) Simulated spectra were used to test the robustness of bathymetry models by isolating the  
 281 effect of IOPs and also to evaluate their performance under optically complex conditions (Section 5-2); (3)  
 282 A WV-2 image was used to map the bathymetry of the Sarca River from space considering both top of  
 283 atmosphere (TOA) and AComp reflectances. A field survey was performed to collect in-situ depths for  
 284 calibration and validation of models (Section 5-3). To perform consistent analyses, the spectral reflectances  
 285 from different sources were convolved with the spectral response functions of the WV-2 and GeoEye  
 286 sensors. The band designations of sensors are given in Table 1.

287 **Table 1.** Spectral band specifications for GeoEye and WV-2 sensors (DigitalGlobe, 2013).

| GeoEye    |                        |                | WV-2              |                        |                |
|-----------|------------------------|----------------|-------------------|------------------------|----------------|
| Band      | Center wavelength (nm) | Bandwidth (nm) | Band              | Center wavelength (nm) | Bandwidth (nm) |
| Blue (B)  | 484                    | 76             | Coastal-Blue (CB) | 427                    | 62             |
| Green (G) | 547                    | 81             | Blue (B)          | 478                    | 73             |
| Red (R)   | 676                    | 42             | Green (G)         | 546                    | 80             |
| NIR       | 851                    | 156            | Yellow (Y)        | 608                    | 48             |
|           |                        |                | Red (R)           | 659                    | 70             |
|           |                        |                | Red Edge (RE)     | 724                    | 50             |
|           |                        |                | NIR1              | 833                    | 136            |
|           |                        |                | NIR2              | 949                    | 187            |

288

289 **5-1- Laboratory Experiments**

290 A set of spectral reflectances was collected in an indoor hydraulic laboratory to test bathymetry models  
 291 under controlled conditions of illumination, water level, IOPs, and bottom properties. These experiments  
 292 are, to the best of our knowledge, the first to integrate spectroscopic and hydraulic facilities in an indoor  
 293 laboratory, although similar experiments have previously been carried out by Legleiter and Overstreet

294 (2014) in an outdoor environment. Two water flumes with different bottom properties were used to examine  
295 depth retrieval from spectral measurements (Fig. 1). Flume-1 was an 18 m long, 1 m wide and 0.7 m high  
296 channel with a layer of uniform fine sand on the bottom. Flume-2 was a 6 m long, 0.4 m wide, and up to  
297 0.4 m deep with a semi-natural substrate consisting of natural sands combined with larger (3 cm diameter)  
298 ball-shape gravels with plastic material. Suspended sediment was considered as the main parameter  
299 defining the water column optical properties due to the fact that sediment load is the primary control on the  
300 IOPs of clear rivers (Legleiter and Overstreet, 2012; Legleiter et al., 2016). SSC was about  $2 \text{ g/m}^3$  whereas  
301 the variation of this parameter was negligible between two flumes.

302 The channels were equipped with a flowmeter to measure the discharge and an adjustable tailgate weir was  
303 located at the end of the flume to control the water level and ensure a uniform flow condition. Experiments  
304 were focused on an area in the longitudinal and cross-sectional middle of each channel to ensure a well-  
305 developed flow and also to mitigate as much as possible the reflections and shadows from the flume  
306 sidewalls. Moreover, two sides of the smaller flume (flume-2) were covered with a low-reflective black  
307 material in the test area to minimize possible side reflections. The water depths were measured using a  
308 point-gage. The spectra were collected by installing over the test area a fiber optic jumper cable connected  
309 to an Analytical Spectral Devices (ASD) HandHeld2 spectroradiometer that allowed measurement of  
310 reflectance in the 325–1075 nm spectral range with 1 nm spectral resolution. Unstable lighting conditions  
311 were eliminated by covering the experiment area on flume-1 while flume-2 was located in a darkroom. A  
312 standard ASD illuminator was used to produce highly stable light across the full spectral range (350 – 2500  
313 nm), which entirely covers the above mentioned operation range of the spectroradiometer. Spectra for a  
314 range of depths were collected from the two flumes by changing the water level in one cm increments. For  
315 each flow condition, three spectra were recorded as the average of 25 individual samples. Dark current and  
316 white reference measurements were taken and updated for each spectral recording in order to convert the  
317 raw spectra into reflectance.

318



319 **Fig. 1.** Spectroscopic experiments in a range of water depths on (a) flume-1 with a sand bed and (b) flume-2 with a  
 320 gravel bed composed of semi-natural material.

### 321 **5-2- Radiative Transfer Simulations**

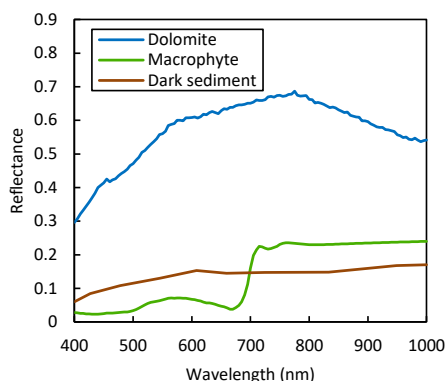
322 Radiative transfer simulations have been used previously to examine the accuracy of OBRA by isolating  
 323 the effects of substrate type and SSC in shallow rivers (Legleiter et al., 2009; Legleiter and Roberts, 2009).  
 324 We performed simulations using the Hydrolight radiative transfer model (Mobley and Sundman, 2008) to  
 325 examine the proposed MODPA by isolating the effect of IOPs by manipulating Chl-a, SSC, and CDOM.  
 326 Long-term measurements of water quality parameters in Italian alpine rivers reported by the Trento  
 327 Environment Protection Provincial Agency (Giardino et al., 2007) were used to define the range of IOPs  
 328 used in the simulations. The relatively wide range of IOPs assumed for radiative transfer simulations  
 329 permitted the evaluation of bathymetric models not only in normal conditions of the Sarca River but also  
 330 in extreme conditions of IOPs (relatively turbid waters). This broader range of IOPs and water depth for  
 331 the simulated data can thus be used to assess the feasibility of extending our approach to other rivers with  
 332 similar optical properties.

333 The effect of each IOP was isolated by considering constant values for the other IOPs (Table 2). Note that  
 334 dolomite, which is dominant bottom type in the Sarca River study region, was considered for these  
 335 simulations and the water depth varied from 2 cm to 2 m in 2 cm increments. For each experiment, 300  
 336 spectral reflectances were simulated for which half of the data, selected at random, were used for calibration  
 337 of the models and the remaining data reserved for validation. The CDOM absorption at 440 nm,  $a_{CDOM}$   
 338 (440), was chosen to quantify the influence of this constituent on this IOP (Kirk, 1996).

339 **Table 2.** The range of IOPs considered for Hydrolight simulations. The effect of variations in each of IOPs was  
 340 isolated by considering constant values for other IOPs.

| Isolated IOP (variable)                            | Other IOPs (constant)   |
|--|---|
| Chl-a = [1, 3, 5] mg/m <sup>3</sup>                | SSC= 3 g/m <sup>3</sup> , $a_{CDOM}(440)= 0.22 \text{ m}^{-1}$    |
| SSC= [0, 3, 6] g/m <sup>3</sup>                    | Chl-a= 3 mg/m <sup>3</sup> , $a_{CDOM}(440)= 0.22 \text{ m}^{-1}$ |
| $a_{CDOM}(440)= [0.07, 0.22, 0.36] \text{ m}^{-1}$ | Chl-a= 3 mg/m <sup>3</sup> , SSC= 3 g/m <sup>3</sup>              |

341  
 342 In addition, an optically-complex condition was also considered to explore the effectiveness of bathymetry  
 343 models by treating all of the IOPs and also the bed type as variable parameters. Three different bottom types  
 344 (dark sediment, macrophyte, and dolomite) were considered in the same range of IOPs and water depths of  
 345 previous simulations, resulting in 8100 individual spectra. Spectral reflectances of the three bottom types  
 346 are shown in Fig. 2 which are characteristics of both bright and dark substrates.



347  
 348 **Fig. 2.** Spectral reflectances of bottom types used in radiative transfer simulations.

349 **5-3- WV-2 Image and In-Situ Measurements**

350 An 8-band WV-2 image and its spectral convolution with GeoEye's band passes (Table 1), were used to  
351 map the bathymetry of the Sarca River. The Sarca is a mountain-piedmont gravel-bed river flowing from  
352 the Adamello glaciers down to Lake Garda in northeast Italy. It is a shallow (depth <1 m), narrow (mean  
353 width < 30 m), and clearly flowing stream which is regulated by an upstream dam that maintains a very  
354 consistent water level with a minimal sediment load during a long period of several years. A WV-2 image  
355 was used for which both TOA and AComp (Pacifici et al., 2014) reflectances were available. AComp  
356 provides an estimate of aerosol optical depth and water vapor independently in each pixel and applies the  
357 atmospheric correction by accounting for adjacency effects (Pacifici, 2016; DigitalGlobe, 2016). In  
358 addition, we spectrally convolved the WV-2 image with the spectral response function of the GeoEye sensor  
359 to gain more insight into the effectiveness of the additional spectral bands of the WV-2 imagery over  
360 traditional 4-band (RGB-NIR) HRSI like GeoEye for mapping river bathymetry.

361 The field survey was carried out in three reaches along the river to gather depth samples as representative  
362 as possible for different environmental conditions (depth, bottom type, etc.). The in-situ depths were  
363 recorded with precise coordinates using RTK GPS along cross-sections with about one to two meter  
364 distances (Fig. 3). An ordinary block kriging was used to interpolate the measured depths at the pixel scale  
365 to enable a pixel-to-pixel comparison of in-situ depths with the image-derived estimates (Legleiter and  
366 Overstreet, 2012).

367  
368  
369





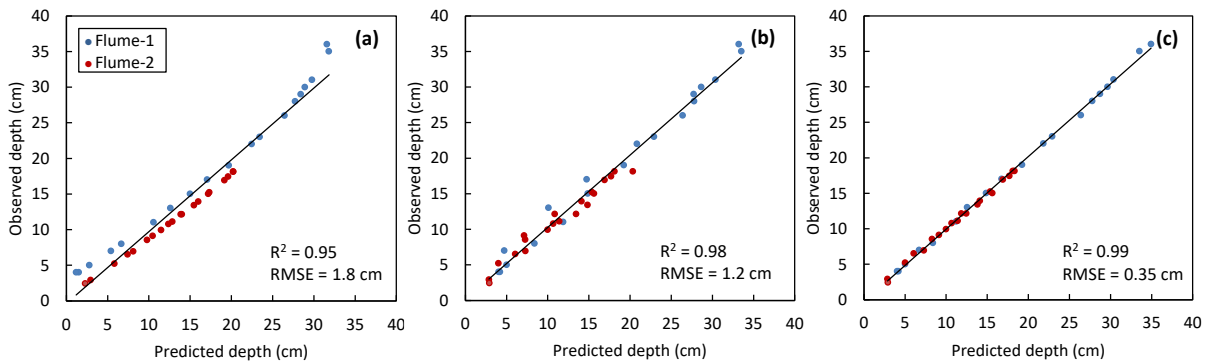
370  
 371 **Fig. 3.** In-situ measurements of water depths in (a) three reaches of the Sarca River, using (b) a RTK GPS (c) at  
 372 dense points along cross-sections. The location of river is highlighted in northeast Italy.

373 **6- Results**

374 The bathymetry models were applied to spectroscopic data collected in the laboratory, synthetic data from  
 375 radiative transfer modeling, and HRSI. Findings are presented and discussed in the following subsections.

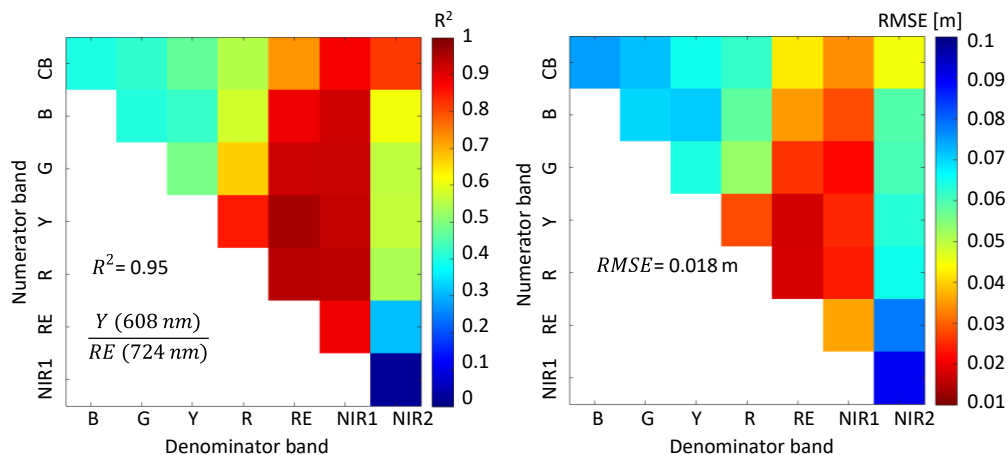
376 **6-1- Laboratory Experiments**

377 The parameters of the bathymetric models were estimated using half of the observations over both flumes,  
 378 selected at random, to gain insight into the robustness of the models with respect to substrate variations  
 379 between the flumes. Fig. 4 represents the predicted vs. observed depths using WV-2 spectra for validation  
 380 samples. For brevity, the match-ups between predicted and observed depths for the simple Lyzenga model  
 381 that provided the lowest accuracies are dropped from all figures but the accuracy statistics are provided on  
 382 bar charts.



383  
 384 **Fig. 4.** Validation of depths derived from (a) OBRA, (b) multiple Lyzenga and (c) MODPA based on PLS regression  
 385 using laboratory spectra convolved to WV-2 bands.

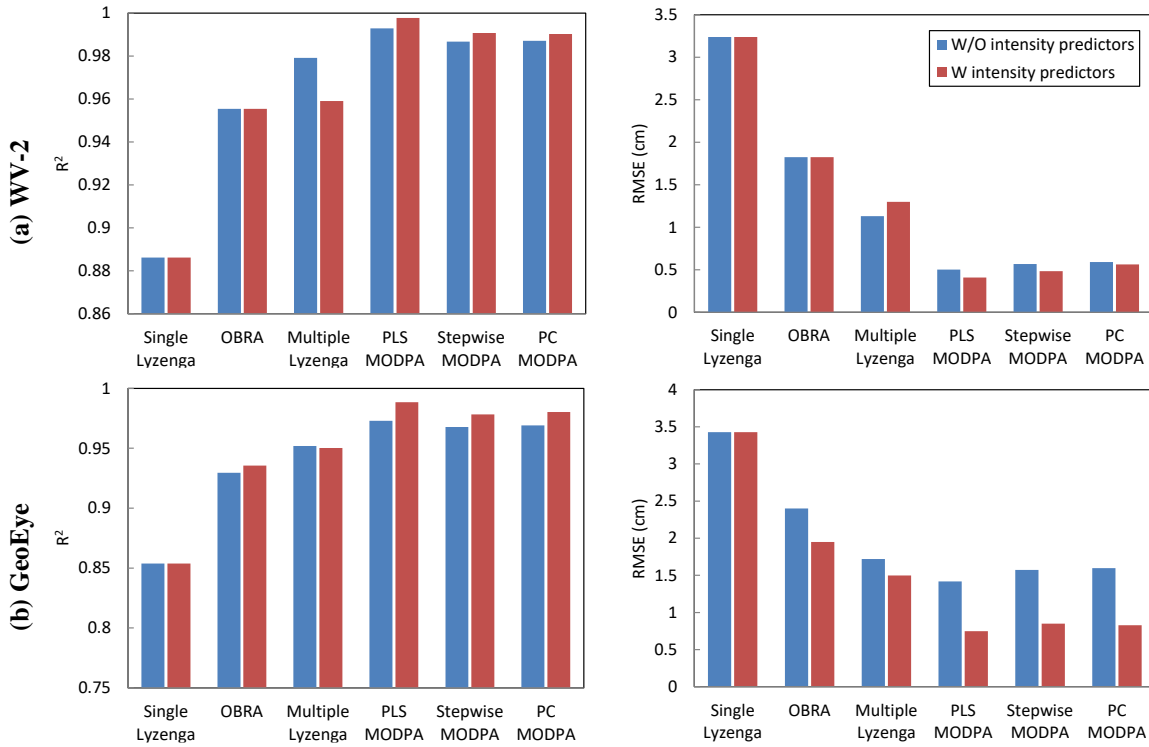
386 The OBRA matrices illustrated in Fig. 5 show the  $R^2$  and RMSE of the ratio model for all possible  
 387 combinations of spectral bands; the highest regression  $R^2$  occurred for the ratio between the yellow and the  
 388 red-edge bands (Y/RE).



389  
 390 **Fig. 5.** OBRA of laboratory WV-2 spectra representing  $R^2$  and RMSE of the ratio bathymetry model for all the  
 391 possible combination of spectral bands.

392 As evident in Fig. 4, the retrievals from OBRA were sensitive to the substrate types of the two flumes. The  
 393 relatively bright substrate in flume-1 has been confused with shallower depths while the darker bottom-  
 394 type of the flume-2 led to overestimation of depths. The multiple Lyzenga model and MODPA were both  
 395 robust with respect to substrate variability. However, the residuals from MODPA were about four times  
 396 smaller than those of multiple Lyzenga (0.35 cm vs. 1.2 cm RMSEs).

397 The accuracy statistics of bathymetry models with and without intensity predictors are compared for the  
 398 laboratory spectra convolved to both WV-2 and GeoEye bands in Fig. 6. The three different regression  
 399 approaches (i.e., PLS, stepwise and PC) provided high accuracies for the proposed MODPA. However,  
 400 MODPA based on PLS regression was slightly more accurate than the other two forms of regression. The  
 401 optimal model, PLS-based MODPA, was composed of one Lyzenga predictor derived from the RE band  
 402 and three ratio predictors derived from G/NIR1, Y/RE and R/RE ratios for the laboratory WV-2 spectra.  
 403 The extra predictors improved the accuracies of bathymetry retrievals. The improvements were more  
 404 pronounced for the spectra convolved to a lower number of bands (i.e., 4-band GeoEye), and we inferred  
 405 that the enhanced spectral resolution of WV-2 led to more accurate depth retrievals than GeoEye.



406 **Fig. 6.** Accuracy statistics ( $R^2$  and RMSE) of bathymetry models with (W) and without (W/O) intensity predictors  
 407 applied to laboratory spectra convolved to match (a) WV-2 and (b) GeoEye bands.

## 408 6-2- Synthetic Data Analysis

### 409 6-2-1- Isolating the Effect of IOPS

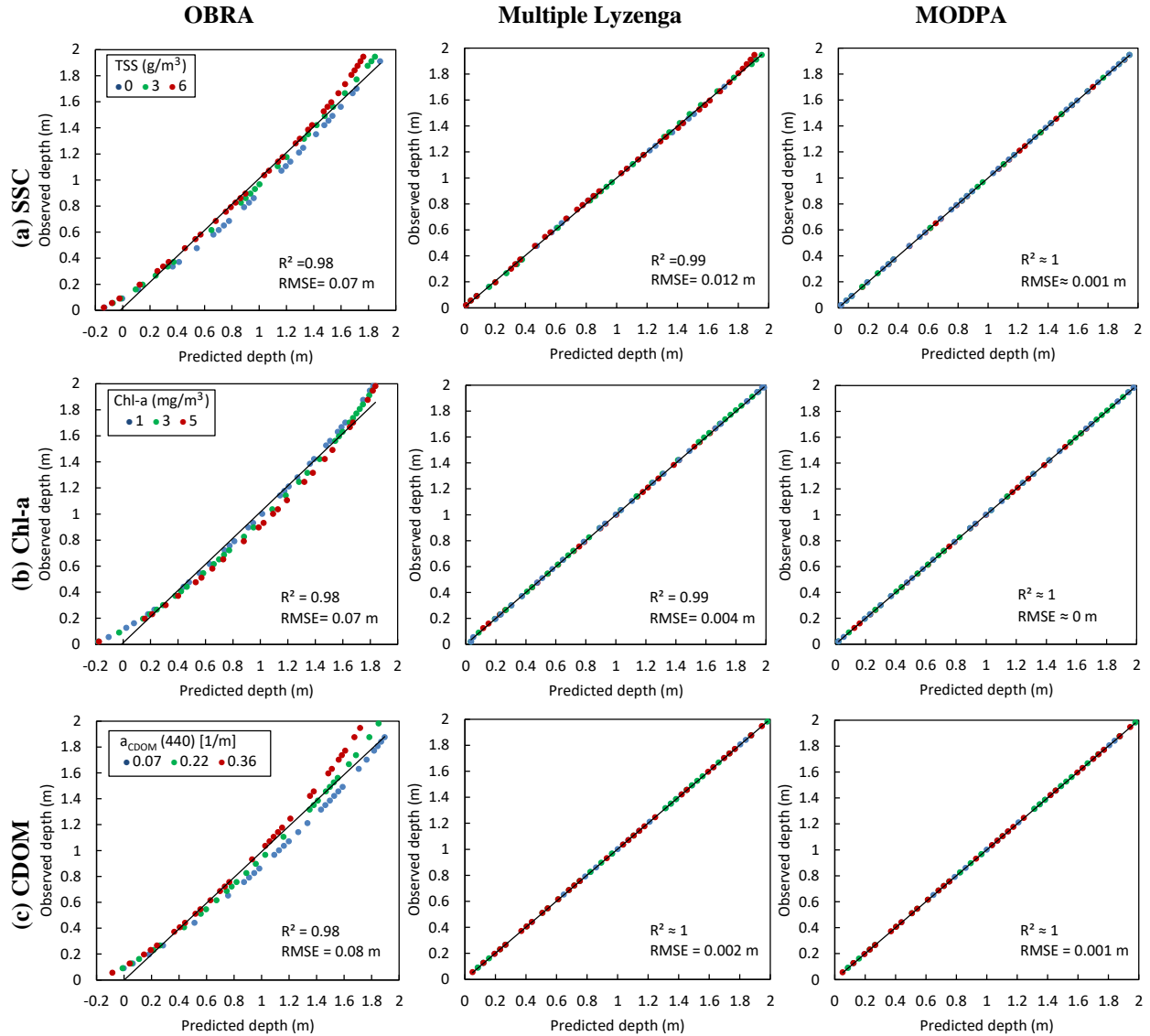
410 Fig. 7 illustrates the results of isolating the effect of variations in IOPs for waters with up to 2 m depth. The  
 411 OBRA-based retrievals were sensitive to changes in concentrations of each IOP. According to Legleiter et  
 412 al. (2009), the exponential relation between radiance and depth is subject to failure as depth increases. This  
 413 is because IOPs, particularly as influenced by SSC, imply greater scattering in a thicker water column. As  
 414 evident in Fig. 7, mismatches between the OBRA retrievals and known depths are more pronounced for the  
 415 higher depths, particularly with high SSC. The multiple Lyzenga model and MODPA showed very good  
 416 performance, but the residuals were smaller for the proposed MODPA.

417

418

419

420

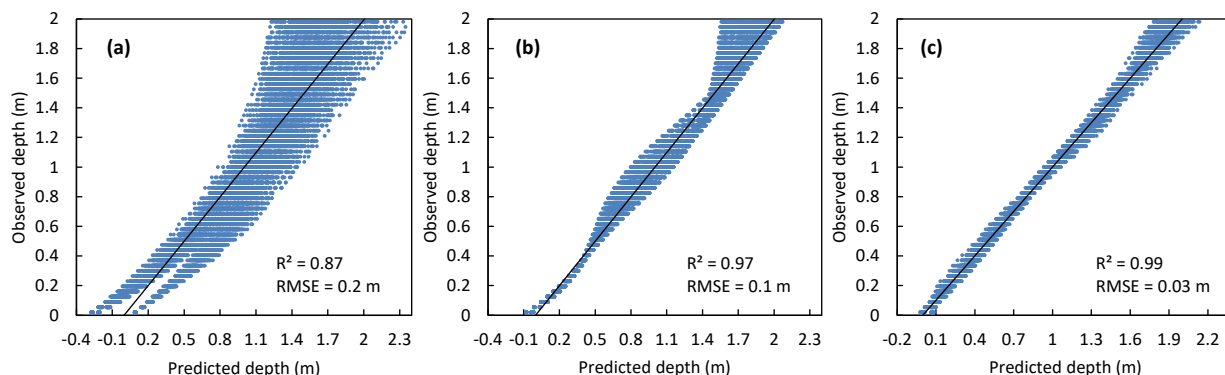


421 **Fig. 7.** Match-up validation of different bathymetry models by isolating the effect of IOPs including (a) SSC, (b)  
 422 Chl-a, and (c) CDOM.

### 423 6-2-2- Optically-Complex Shallow Waters

424 In this testing strategy, we have assumed shallow waters with variable bottom-types and IOPs (see Section  
 425 5-2). MODPA led to the highest correlation with known depths ( $R^2 = 0.98$  and RMSE= 6 cm without  
 426 considering intensity predictors). Including the intensity predictors further enhanced depth retrieval using  
 427 MODPA (RMSE= 3 cm). This demonstrated the effectiveness of intensity predictors for improving the  
 428 robustness of bathymetry models in optically-complex waters. The match-up validations indicated

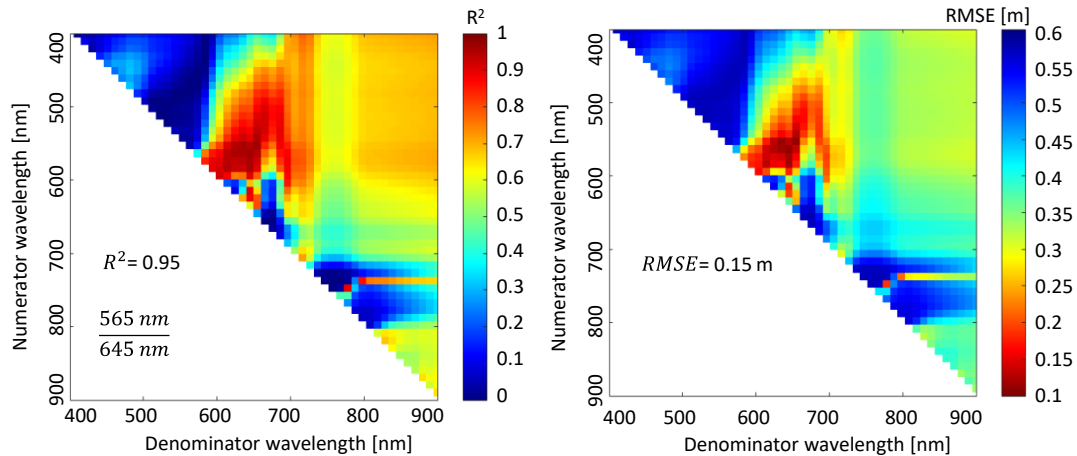
429 significant improvement (i.e., 7 cm better RMSE) of depth retrieval using MODPA compared to the  
430 multiple Lyzenga model (Fig. 8).



431  
432 **Fig. 8.** Match-up validation of depth retrieval based on (a) OBRA, (b) Multiple Lyzenga and (c) MODPA with

433 intensity predictors for the optically complex spectra with variable IOPs and bottom types.

434 We performed further analysis to understand if hyperspectral data could improve the performance of OBRA  
435 in the optically-complex testing scenario. Radiative transfer simulations with a spectral resolution of 10 nm  
436 were used to perform OBRA in the spectral range of 400 nm to 900 nm. As evident in Fig. 9, depth retrieval  
437 for the optimal pair of ratio bands has been improved compared to that of 8-band WV-2 data, but required  
438 very high spectral resolution (i.e., 50 bands in the range of 400 nm to 900 nm). However, the results are not  
439 comparable with MODPA (RMSE of 3 cm for MODPA vs. 15 cm for OBRA using hyperspectral data).  
440 This indicates that utilizing multiple predictors derived from a relatively low spectral resolution data (8-  
441 band WV-2) through MODPA is much more effective than when using a single predictor model like OBRA,  
442 even with high spectral resolution. Note that the wavelength position rather than the spectral resolution of  
443 hyperspectral data can also influence the performance of OBRA (Legleiter et al., 2009).



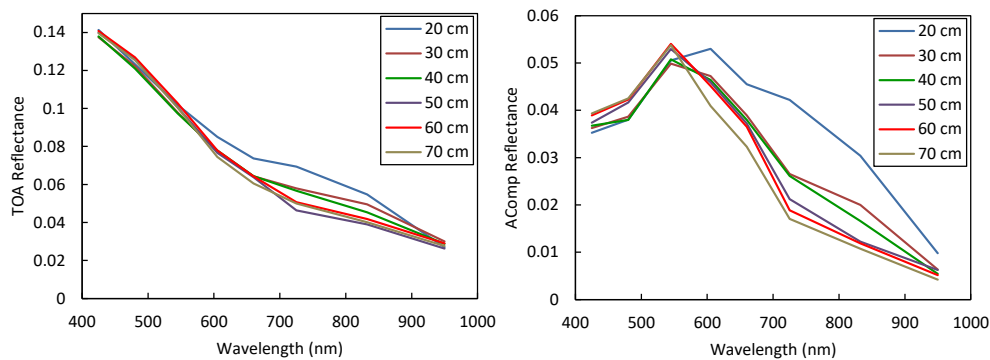
444

445 **Fig. 9.** OBRA of simulated spectra with 10 nm spectral resolution for the optically-complex testing scenario.

446 **6-3- WV-2 Image Analysis**

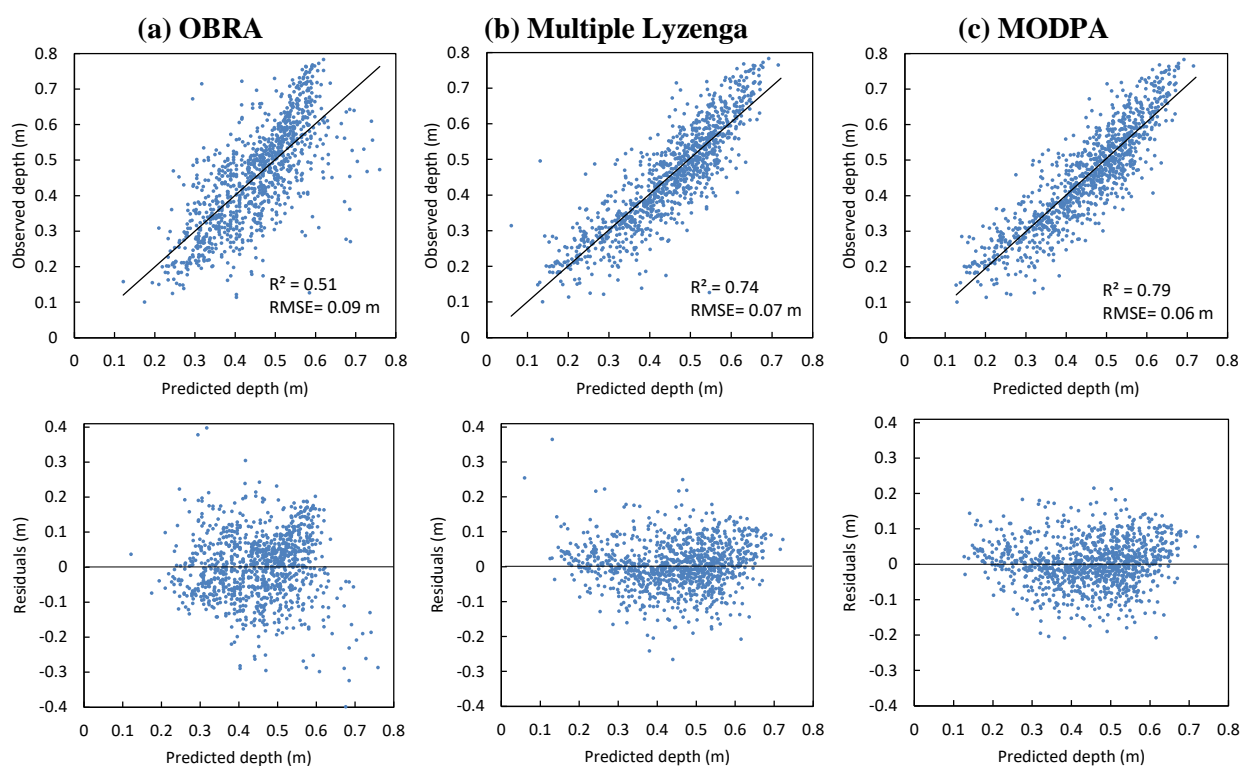
447 Atmospheric effects can make a significant contribution to the TOA radiance at short wavelengths (mainly  
 448 visible bands) due to the low reflectivity of water bodies (Gordon, 1990; Pahlevan et al., 2017). Fig. 10  
 449 compares the AComp reflectances (i.e., surface reflectances) with TOA reflectances for WV-2 image pixels  
 450 from a range of water depths along the Sarca River. The image-derived reflectances were averaged for all  
 451 pixels with a given depth known from the field survey. As evident in Fig. 10, atmospheric effects were  
 452 significant at short wavelengths dominated by Rayleigh scattering (Gordon 1990; Pahlevan et al., 2017).  
 453 AComp and TOA reflectances of the WV-2 image were then supplied to the bathymetry models to  
 454 investigate robustness of the models with respect to atmospheric effects.

455



456 **Fig. 10.** Comparison of TOA and AComp reflectances of WV-2 image in a range of water depths along the Sarca  
 457 River.  
 458

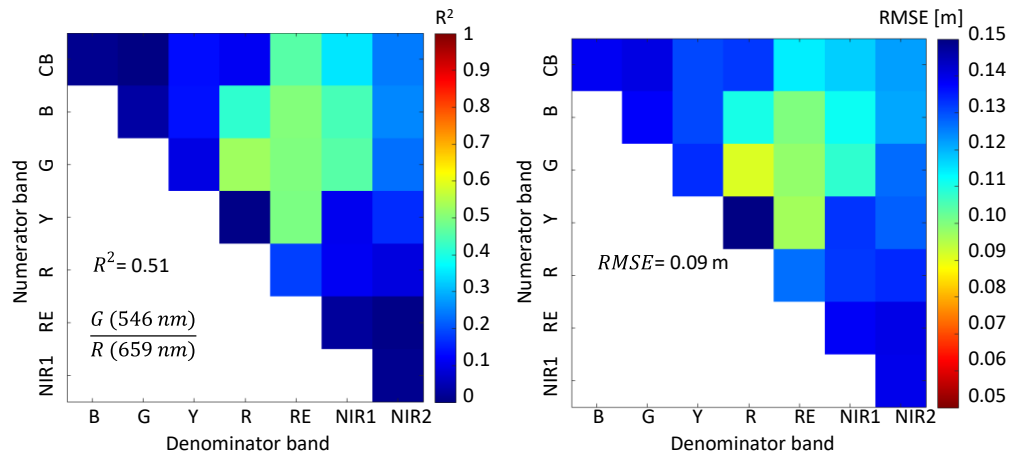
459 As first validation approach, one half of the data was reserved for calibration of models and the remaining  
 460 half for accuracy assessment. Note that substrate compositions such as algae cover and also water column  
 461 constituents can vary over distances of less than a meter in small rivers such as our case study (Fonstad and  
 462 Marcus, 2005), which can significantly complicate the depth retrieval. Fig. 11 illustrates the validation of  
 463 bathymetry models based on TOA reflectances from the WV-2 image; MODPA provided the highest  
 464 accuracy. The residual plots indicate absolute errors of up to 0.4 m for OBRA and multiple Lyzenga  
 465 methods, whereas MODPA provided depth estimates with residuals smaller than 0.2 m.



466 **Fig. 11.** Validation of depth retrieval from TOA reflectances of WV-2 image based on (a) OBRA, (b) Multiple  
 467 Lyzenga and (c) MODPA using PLS regression.

468 Fig. 12 shows the OBRA matrix obtained from TOA reflectances of WV-2 image for which G/R ratio  
 469 yielded the highest observed vs. predicted  $R^2$  (0.51) with an RMSE of 9 cm. The matrix indicates that band  
 470 ratios with a B or G numerator and a RE or NIR1 denominator as well as Y/RE ratio also provided  
 471 comparable results with the optimal band ratio (i.e., G/R). This demonstrates the potential of long  
 472 wavelengths across the near-infrared spectrum in retrieving the bathymetry in shallow and clear waters as

473 long as the water column depth is not too great and the IOPs do not dictate complete absorption or scattering  
 474 of the signal.



475  
 476 **Fig. 12.** OBRA using TOA reflectances of WV-2 image representing  $R^2$  and RMSE of the ratio model for all the  
 477 possible combination of spectral bands.

478 Fig. 13 shows the retrieved bathymetry maps from TOA reflectances compared to in-situ depths along three  
 479 reaches of the Sarca River.

480

481

482

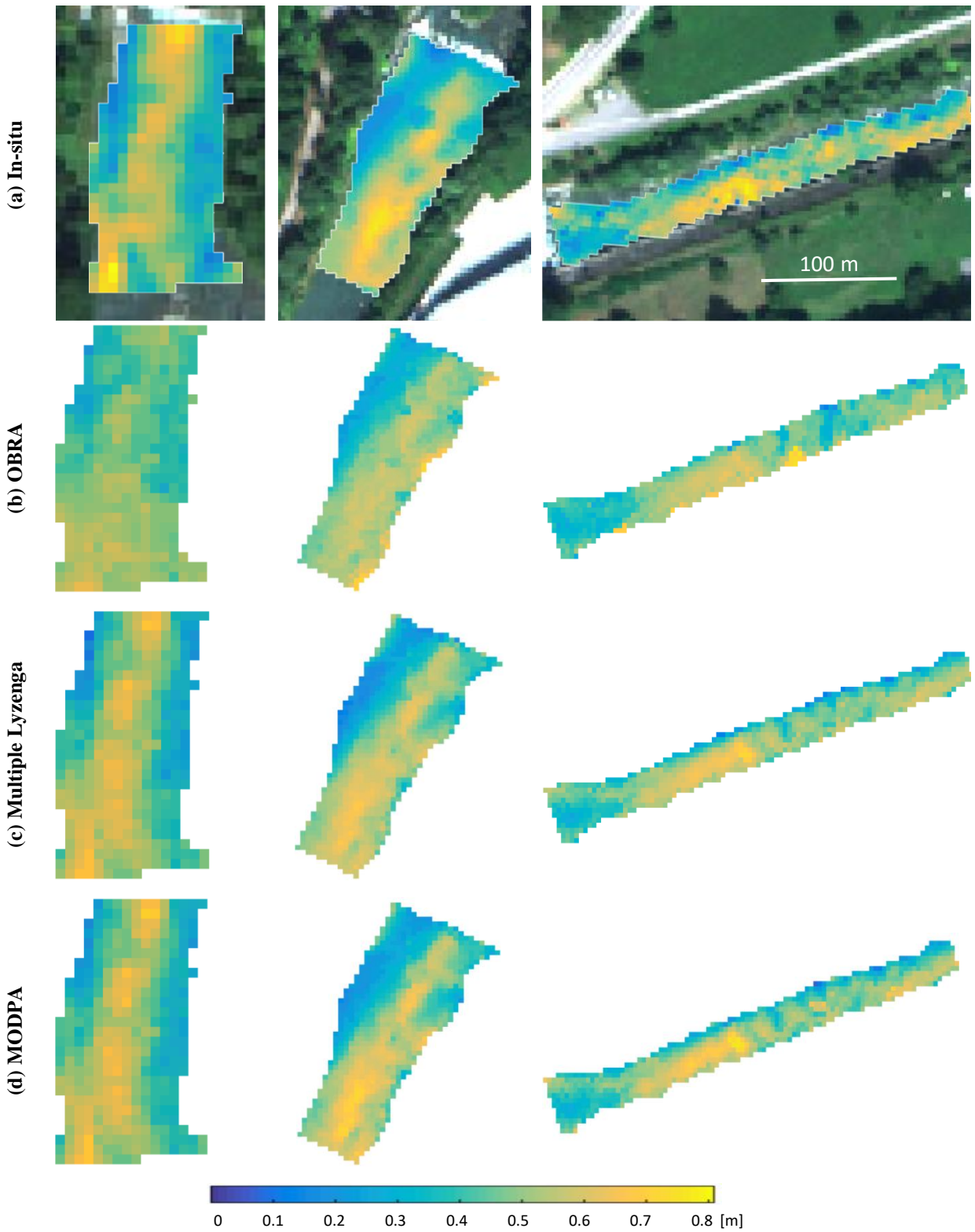
483

484

485

486





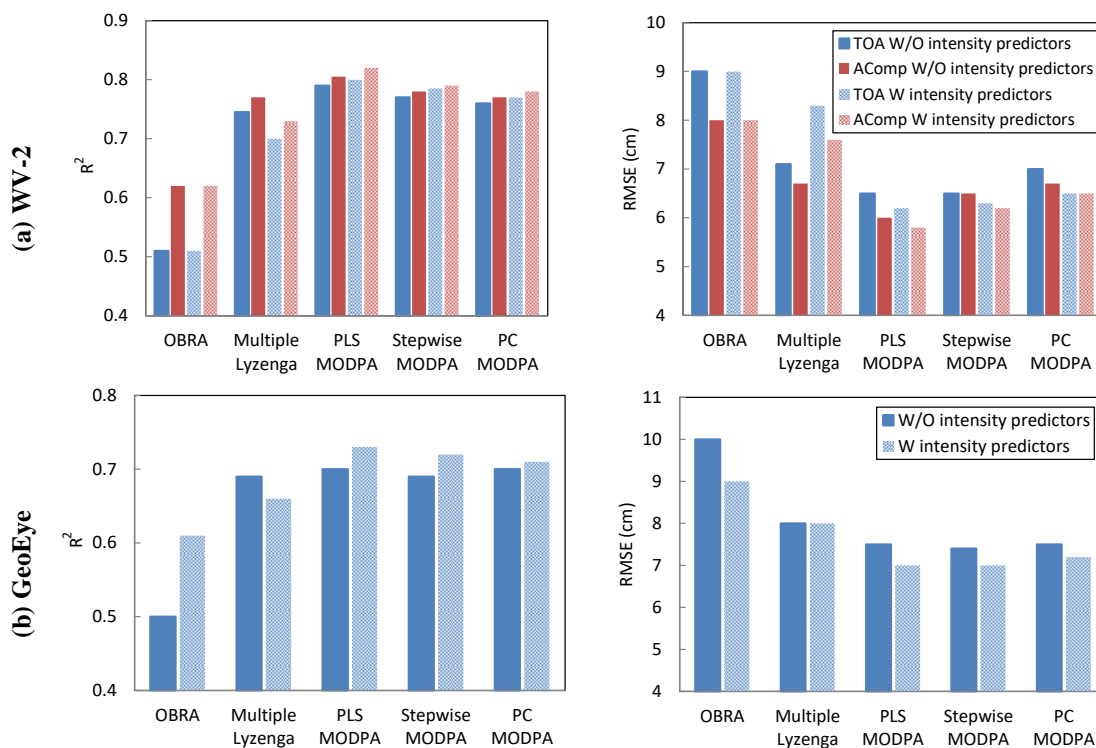
487

488

489

**Fig. 13.** Comparison of (a) in-situ depths with bathymetry maps derived from (b) OBRA, (c) Multiple Lyzenga model and (d) MODPA.

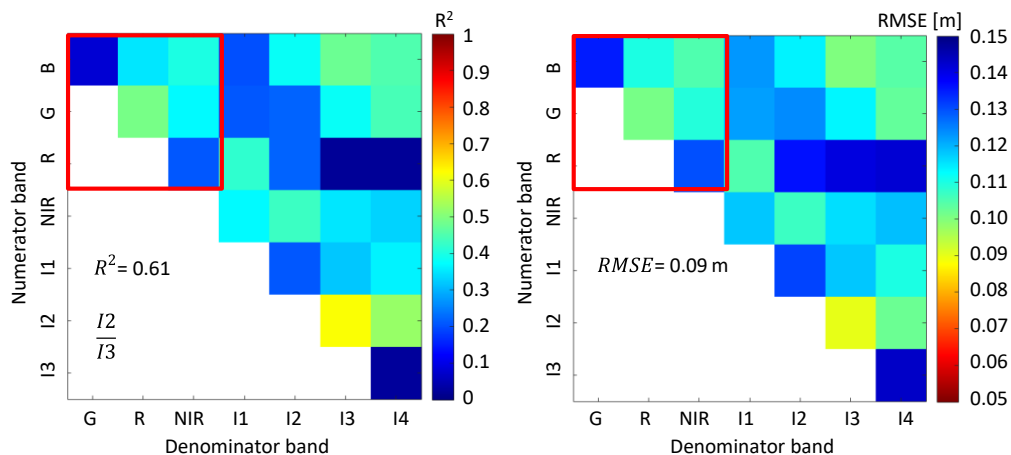
490 The accuracy statistics of bathymetry models with and without intensity predictors are compared for the  
 491 WV-2 image and its convolution to GeoEye bands in Fig. 14. In addition, AComp reflectances were  
 492 examined relative to the TOA reflectances using the WV-2 image. In general, the AComp reflectances  
 493 yielded higher accuracies than TOA reflectances. However, the accuracy enhancement was more  
 494 pronounced for OBRA, whereas MODPA was less affected by atmospheric effects. Again, the three  
 495 approaches for selection of optimal predictors provided comparable results, but the PLS regression was  
 496 slightly more accurate than the others. This model was composed of three Lyzenga predictors derived from  
 497 CB, G and RE bands and two ratio predictors derived from G/R and G/NIR1 using the WV-2 image.



498 **Fig. 14.** Accuracy statistics ( $R^2$  and RMSE) of bathymetry models with (W) and without (W/O) intensity predictors  
 499 applied on (a) WV-2 and (b) GeoEye images. The comparison also performed for the TOA and AComp reflectances  
 500 of the WV-2 image.

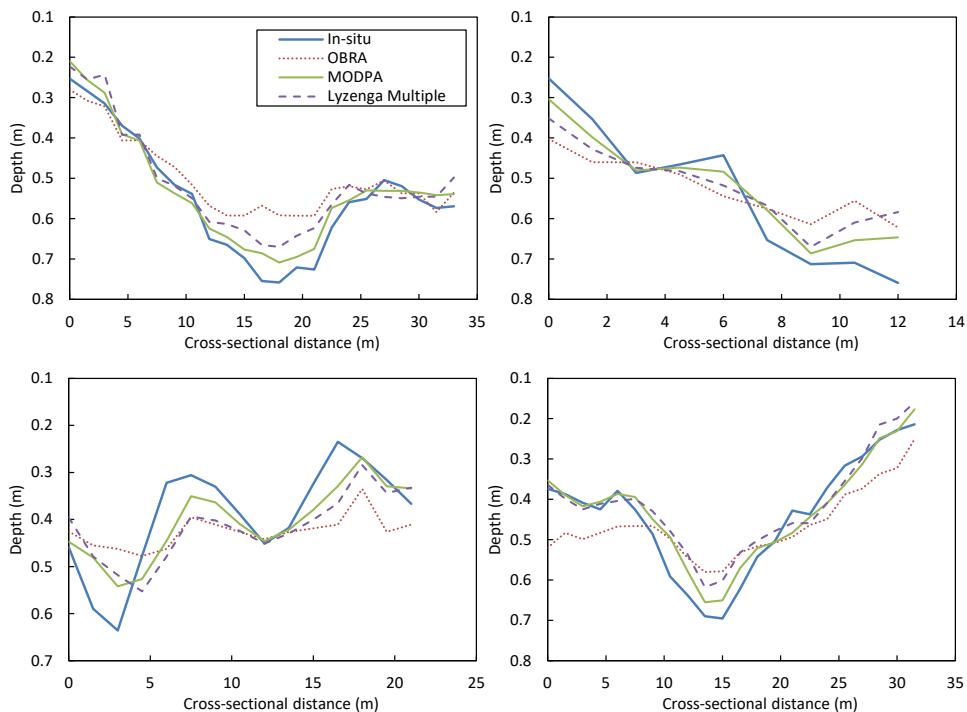
501 As can be inferred from Fig. 14, the intensity predictors in general led to an increase of  $R^2$  for all the models  
 502 except for the Lyzenga's multiple regression model. This is mainly because making use of all the Lyzenga  
 503 predictors derived from original bands and intensity components induces the overfitting problem as well as  
 504 degradation of predictive power due to the presence of irrelevant predictors. As an interesting point,

505 intensity predictors for the GeoEye image remarkably increased the accuracy of OBRA (about 0.1  
 506 enhancement of  $R^2$ ). This is shown in Fig. 15 where the optimal ratio model has been derived from intensity  
 507 (I) bands.



508 **Fig. 15.** OBRA of GeoEye image where the OBRA matrix derived from the original image bands (RGB color space)  
 509 is highlighted with a red box. The optimal band ratio model was derived from intensity (I) predictors.  
 510

511 Fig. 16 compares the bathymetry retrieved from the WV-2 image with in-situ observations along a few  
 512 randomly selected cross-sections.

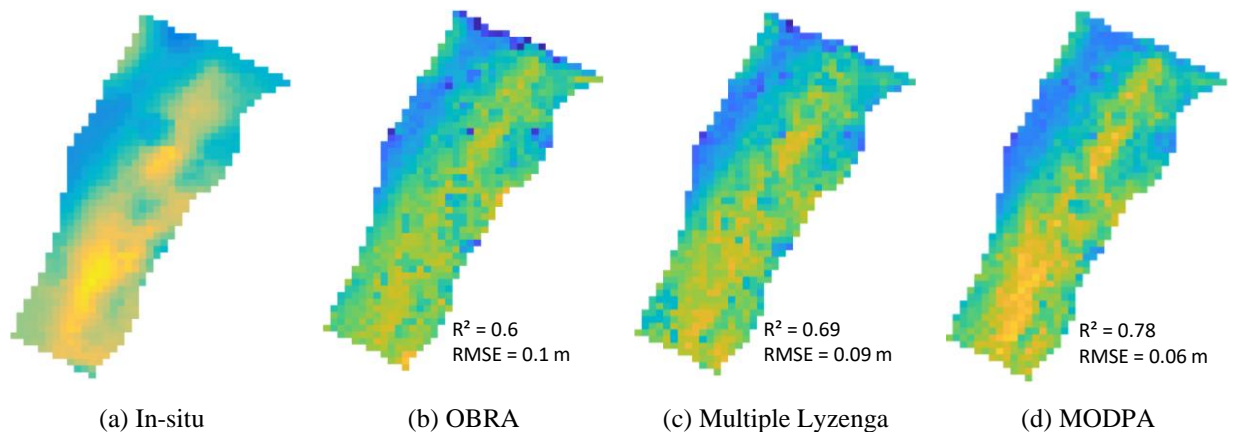


513

514

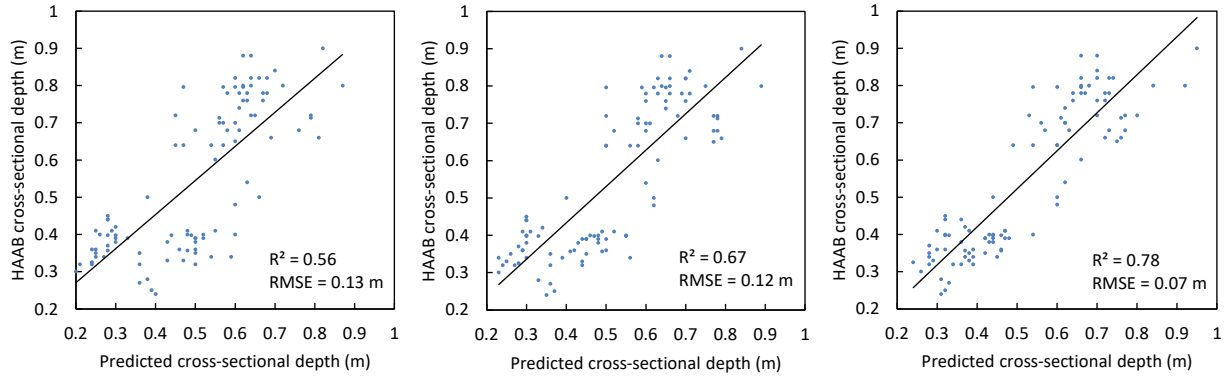
515 **Fig. 16.** Comparison of in-situ depths along cross-sections of the Sarca River with bathymetry retrieval from different  
516 models considering intensity predictors using WV-2 image.

517 We performed an additional analysis to investigate the performance of bathymetry models with spatially  
518 distant samples for calibration and validation. In this context, the two distal in-situ reaches were used for  
519 calibration and the middle one for validation. Fig. 17 shows the depth maps and the accuracy statistics  
520 derived from bathymetric models for the middle reach of the Sarca River. The results demonstrated the  
521 increased validity and robustness of MODPA compared to other methods.



522 **Fig. 17.** Depth maps estimated for the middle reach of the Sarca River by calibrating the bathymetry models with two  
523 distal in-situ reaches.

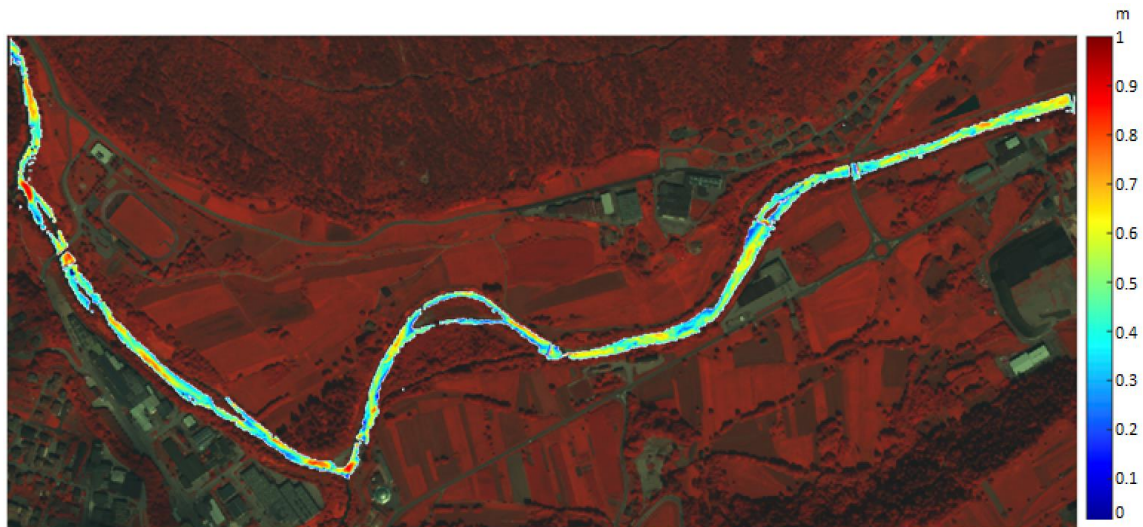
524 In addition, we estimated mean and maximum depths for 50 cross-sections regularly spaced along a 3 km  
525 reach of the Sarca River to perform HAAB (Eqs. 10 and 11). In this regard, the discharge of the river was  
526 available from gage records ( $Q = 4.6 \text{ m}^3/\text{s}$ ). Regional slopes of the channel were estimated from an available  
527 LiDAR-derived digital surface model ( $0.01 < S < 0.003$ ) and cross-sectional widths ( $W$ ) were measured on  
528 the image. The depth estimates based on HAAB allowed us to perform an independent analysis on the  
529 efficacy of bathymetry models in reaches where no in-situ measurement was available. The proposed  
530 MODPA resulted in a more accurate depth estimates compared to OBRA and multiple Lyzenga models.  
531 MODPA-based depth estimates indicate enhancement of  $R^2$  on the order of 0.22 and 0.11 with RMSE  
532 improvement of 0.06 m and 0.05 m compared to OBRA and multiple Lyzenga models, respectively (Fig.  
533 18).



534

535 **Fig. 18.** Mean and maximum cross-sectional depths from HAAB compared with depth retrievals from WV-2 image  
 536 based on (a) OBRA, (b) Multiple Lyzenga and (c) MODPA using PLS regression.

537 The bathymetric map derived from the WV-2 image for a 5 km-long reach using the proposed MODPA  
 538 based on PLS regression is shown in Fig. 19. In addition to the quantitative assessment performed on  
 539 independent check points described above, visual inspection also supports the realism of the map, with the  
 540 pool-to-pool spacing across the reach corresponding to the theoretically established 5-7 channel widths  
 541 (Montgomery et al., 1995).



542

543 **Fig. 19.** Bathymetry map derived from the proposed MODPA based on PLS regression using WV-2 image.

544 **7- Discussion**

545 Lyzenga’s single predictor demonstrated to be very sensitive to variations in substrate type and IOPs.  
 546 Although this predictor individually failed in providing depth information, it might have potential for  
 547 classifying riverbed compositions. The OBRA also failed to provide satisfactory, robust depth retrieval with

548 respect to substrate and IOPs variability. Despite identification of the optimal pair of bands for the ratio  
549 model, OBRA is a single predictor model and most likely neglects other explanatory variables even when  
550 using very high spectral resolution data. Multiple Lyzenga predictors enhanced the robustness of the model  
551 with respect to optically complicating factors in riverine environments. However, this model does not  
552 account for any process to select optimal predictors and might lead to overfitting problems that could  
553 degrade prediction accuracies due to the risk of correlated and redundant predictors. This problem would  
554 become even more significant when using high-dimensional (hyperspectral) imagery and also when  
555 considering additional candidate predictors such as intensity components used in this study. The  
556 performance of the multiple Lyzenga model on WV-2 data was degraded by including the intensity  
557 predictors. This finding highlights the significance of using MODPA to identify optimal predictors, among  
558 all the candidate predictors, including the intensity components. Moreover, intensity predictors were most  
559 significant when there were more complexities in the data (Fig. 8). This is reasonable as the main rationale  
560 for adding new predictors is to deal with complex data and enhance robustness with respect to all  
561 undesirable variations. As OBRA and proposed MODPA identify the optimal predictor/s, they yielded  
562 improved results when using intensity predictors. More specifically, the single predictor of OBRA for the  
563 GeoEye image was a combination of intensity predictors. This result shows the effectiveness of extra  
564 predictors such as intensity components for bathymetry mapping from imagery with low spectral resolution.  
565 The results of bathymetry models applied to simulated spectra further suggested the robustness of MODPA  
566 with respect to changes in IOPs (as influenced by SSC, Chl-a and CDOM) and also in optically-complex  
567 rivers where all the IOPs as well the bottom types were variable. The intensity predictors improved the  
568 results of MODPA in the testing scenario associated with the simulated optically-complex rivers (3 cm  
569 improvement of RMSE for depths up to 2 m). Moreover, the range of predicted depths for MODPA was  
570 more in agreement with the known depths whereas other methods were hindered by estimation of some  
571 negative depths in the optically-complex testing scenario (see Fig. 8).

572 The enhanced spectral resolution of WV-2 showed benefits for mapping the bathymetry of shallow rivers.  
573 For instance, the long-wavelength bands including RE and NIR1 proved to be useful as Lyzenga predictors  
574 or as the denominator of ratio-based predictors. This is mainly because light in shallow and clear rivers is  
575 not fully attenuated even for long/highly-absorbing wavelengths. On the other hand, short-wavelength  
576 bands (e.g. B, CB, G and Y) performed as appropriate numerator bands for ratio predictors. In summary,  
577 the WV-2 sensor provided a wealth of options for selecting either Lyzenga or ratio predictors and led to  
578 higher accuracies than when using 4-band GeoEye data (e.g., improvements of  $R^2$  and RMSE respectively  
579 on the order of 9% and 1 cm using TOA reflectances without intensity predictors). Comparing the TOA  
580 and AComp reflectances over a range of field-measured depths showed reasonable correction of  
581 atmospheric effects (e.g., appropriate removal of Rayleigh scattering over short wavelengths). AComp  
582 reflectances yielded higher accuracies than TOA data, with a more pronounced difference for OBRA  
583 (improvements of  $R^2$  and RMSE on the order of 11% and 1 cm, respectively). However, multiple-predictor  
584 models, particularly MODPA, showed robust bathymetry retrievals with respect to atmospheric effects.  
585 MODPA provided promising results and improvements for bathymetry retrieval in the Sarca River based  
586 on a WV-2 image. The best result was derived from MODPA based on PLS regression using AComp  
587 reflectances where  $R^2$  and RMSE were estimated as 0.82 and 5.8 cm, respectively. Although the three  
588 investigated regression methods provided very comparable results, the PLS-based regression showed  
589 slightly more accurate results. The imaged-derived bathymetry of the Sarca River validated based on two  
590 different sampling strategies for calibration of the models and also by comparing with the cross-sectional  
591 depth estimates from basic models of river hydraulics (i.e., HAAB).

## 592 **8- Conclusions and Future Work**

593 The thinner and less complex water columns of shallow and clearly flowing rivers permit the bottom  
594 component of radiance to dominate the signal reaching the sensor. Although this radiance component is  
595 desired for bathymetry retrieval, it is affected not only by water depth but also by substrate type/composition  
596 and indirectly by water column properties (IOPs). Moreover, other factors such as highly variable roughness

597 of the water surface, variable IOPs, and atmospheric effects can complicate depth retrieval in riverine  
598 environments. Therefore, development of methods robust to all these variations is essential in order to  
599 retrieve consistent bathymetric data over large spatial and temporal extents using optical imagery. This  
600 research introduced MODPA to take advantage of both Lyzenga and ratio predictors and also to integrate  
601 extra predictors obtained from the intensity component of the HSI color space. In this regard, all the possible  
602 Lyzenga and ratio predictors derived from the original image as well as the intensity components were  
603 considered as candidate predictors. A set of optimal predictors were then selected based on one of PLS, PC  
604 or stepwise regressions.

605 The proposed MODPA outperformed widely-used OBRA and multiple Lyzenga methods through three  
606 independent analyses using laboratory spectra, radiative transfer model simulations, and satellite data. The  
607 significance of MODPA was demonstrated in optically-complex waters by providing robust retrievals with  
608 respect to variations in substrate type, IOPs, water surface roughness, and atmospheric effects. Additional  
609 predictors (e.g. spectral water indices) could be included in the MODPA particularly for low spectral  
610 resolution imagery or for studies on optically-complex waters, which will be the subject of future  
611 investigations. The radiative transfer simulations were representative of a wide range of IOPs in the study  
612 region, including turbid waters. However, more research should be dedicated to study turbid rivers to further  
613 explore the potential of MODPA. The first tests on DigitalGlobe AComp indicated the effectiveness of this  
614 product for mapping the bathymetry of shallow and clearly flowing rivers. However, more studies should  
615 be dedicated to comprehensively analyze the quality of AComp product for remote sensing of inland waters.

616 Note that the key for empirical depth retrieval methods is to have a sufficient number of samples available  
617 for calibration to allow the regression model to capture the variability and complexity of the data. In the  
618 cases with limited number of in-situ samples, cross-validation approaches (Martens and Dardenne, 1998)  
619 and also the hydraulic-based approach considered in this study (i.e., HAAB) would be beneficial to perform  
620 the calibration and validation of bathymetric models. Moreover, HAAB allows to examine the reliability  
621 of depth retrievals in the reaches without available in-situ depths.



622 This research demonstrated the effectiveness of spectroscopic experiments in an indoor environment of a  
623 hydraulic laboratory to study the bathymetry of very shallow waters considering variable bottom types.  
624 Experiments of this kind can be extended to study other attributes of fluvial systems such as flow velocity  
625 and water quality indicators. The proposed MODPA was demonstrated to be an efficient technique for  
626 mapping river bathymetry. However, application of this technique is restricted neither to riverine  
627 environments nor to a specific optical sensor. MODPA has the potential for application to any multi/hyper-  
628 spectral image over optically shallow inland or coastal waters. The sensor and platform type can be defined  
629 based on requirements of the case study, such as the spatial resolution. Further assessment of MODPA  
630 using freely-available Sentinel-3, Sentinel-2, and Landsat-8 imagery would be interesting in various  
631 coastal/inland applications.

### 632 **Acknowledgments**

633 This work was carried out within the SMART Joint Doctorate (Science for the MAnagement of Rivers and  
634 their Tidal systems) funded with the support of the Erasmus Mundus programme of the European Union.  
635 The authors acknowledge the imagery grant awarded by DigitalGlobe Foundation for providing the WV-2  
636 imagery. We acknowledge the Alexander Goetz instrument support program of ASD Inc. for awarding us  
637 a short-term usage of HandHeld2 spectroradiometer. The authors are grateful to Prof. Aronne Armanini,  
638 Prof. Maurizio Righetti and Prof. Guido Zolezzi for giving access to the hydraulic laboratory at the  
639 University of Trento and their supports during the experiments. We would like to greatly appreciate Dr.  
640 Nima Pahlevan at NASA Goddard Space Flight Center (GSFC) for providing the Hydrolight simulations.  
641 We also highly appreciate constructive comments from Dr. Patrice Carbonneau and two other anonymous  
642 reviewers, which improved the manuscript.

643

### 644 **References**

645 Abdi, H., 2003. Partial Least Square Regression (PLS Regression). In Encyclopedia of Social Science Research  
646 Methods; SAGE: Thousand Oaks, CA, USA, pp. 792–795.

647 Bramante, J.F., Raju, D.K., and Sin, T.M., 2013. Multispectral derivation of bathymetry in Singapore's shallow, turbid  
648 waters, *International Journal of Remote Sensing*, 34:6, 2070-2088.

649 Brando , V.E., Anstee, J.M., Wettle, M., Dekker, A.G., Phinn, S.R., Roelfsem, C., 2009. A physics based retrieval and  
650 quality assessment of bathymetry from suboptimal hyperspectral data. *Remote Sensing of Environment*, 113,  
651 755–770.

652 Bryant, R.G., Gilvear, D.J., 1999. Quantifying geomorphic and riparian land cover changes either side of a large flood  
653 event using airborne remote sensing: River Tay, Scotland. *Geomorphology*, 29 (3/4): 307–321.

654 Carbonneau, P., Fonstad, M.A., Marcus, W.A., Dugdale, S.J., 2012. Making riverscapes real. *Geomorphology*, 137  
655 (1), 74–86.

656 Carbonneau, P.E., Lane, S.N., Bergeron, N., 2006. Feature based image processing methods applied to bathymetric  
657 measurements from airborne remote sensing in fluvial environments. *Earth Surface Processes and Landforms*,  
658 31, 1413–1423.

659 Carbonneau, P.E., Lane, S.N., Bergeron, N.E., 2004. Catchment-scale mapping of surface grain size in gravel bed  
660 rivers using airborne digital imagery, *Water Resources Research*, 40 (7).

661 Carper, W.J., T. M. Lillesand, and R. W. Kiefer, 1990. The Use of Intensity-Hue-Saturation Transformations for  
662 Merging SPOT Panchromatic and Multispectral Image Data, *Photogrammetric Engineering & Remote Sensing*,  
663 56(4):459-467.

664 Dekker, A.G., Phinn, S.R., Anstee, J., Bissett, P., Brando, V.E., Casey, B., Fearn, P., Hedley, J., Klonowski, W., Lee,  
665 Z.P., Lynch, M., Lyons, M., Mobley, C.,Roelfsema, C., 2011. Intercomparison of shallow water bathymetry,  
666 hydro-optics, and benthos mapping techniques in Australian and Caribbean coastal environments. *Limnol.*  
667 *Oceanogr. Methods*, 9, 396–425.

668 Dierssen, HM, Zimmerman, RC, Leathers, RA, Downes, TV, Davis, CO. 2003. Ocean color remote sensing of  
669 seagrass and bathymetry in the Bahamas Banks by high-resolution airborne imagery. *Limnology and*  
670 *Oceanography*, 48: 444–455.

671 Dietrich, J.T., 2017. Bathymetric Structure-from-Motion: extracting shallow stream bathymetry from multi-view  
672 stereo photogrammetry. *Earth Surface Processes and Landforms*, 42: 355–364.

673 DigitalGlobe, 2013. spectral Response for DigitalGlobe Earth Imaging Instruments. Available at: [https://dg-cms-](https://dg-cms-uploads-production.s3.amazonaws.com/uploads/document/file/105/DigitalGlobe_Spectral_Response_1.pdf)  
674 [uploads-production.s3.amazonaws.com/uploads/document/file/105/DigitalGlobe\\_Spectral\\_Response\\_1.pdf](https://dg-cms-uploads-production.s3.amazonaws.com/uploads/document/file/105/DigitalGlobe_Spectral_Response_1.pdf),  
675 Last access on 14/6/2018.

676 DigitalGlobe, 2016. DigitalGlobe Atmospheric Compensation. Available online: [http://digitalglobe-](http://digitalglobe-marketing.s3.amazonaws.com/files/documents/AComp_WP_ACOMP.pdf)  
677 [marketing.s3.amazonaws.com/files/documents/AComp\\_WP\\_ACOMP.pdf](http://digitalglobe-marketing.s3.amazonaws.com/files/documents/AComp_WP_ACOMP.pdf) (accessed on 14 June 2018).

678 Durand, M., Gleason, C. J., Garambois, P. A., Bjerklie, D., Smith, L. C., Roux, H., Rodriguez, E., Bates, P.D., Pavelsky,  
679 T.M., Monnier, J., Chen, X., Di Baldassarre, G., Fiset, J.M., Flipo, N., Frasson, R.P.d.M., Fulton, J., Goutal, N.,  
680 Hossain, F., Humphries, E., Minear, J.T., Mukolwe, M.M., Neal, J.C., Ricci, S., Sanders, B.F., Schumann, G.,

681 Schubert, J. E., and Vilmin, L., 2016, An intercomparison of remote sensing river discharge estimation  
682 algorithms from measurements of river height, width, and slope, *Water Resources Research*, 52, 4527–4549.

683 Flener, C., 2013. Estimating deep water radiance in shallow water: adapting optical bathymetry modeling to shallow  
684 river environments. *Boreal Environment Research*. 18: 488–502.

685 Flener, C., Lotsari, E., Alho, P., Käyhkö, J., 2012. Comparison of empirical and theoretical remote sensing based  
686 bathymetry models in river environments. *River Research and Applications*, 28 (1), 118-133.

687 Flener, C., Vaaja, M., Jaakkola, A., Krooks, A., Kaartinen, H., Kukko, A., Kasvi, E., Hyypä, H., Hyypä, J., and Alho,  
688 P., 2013, Seamless Mapping of River Channels at High Resolution Using Mobile LiDAR and UAV-  
689 Photography. *Remote Sensing*, 5, 6382-6407.

690 Fonstad, M. A., and Marcus, W. A., 2005. Remote sensing of stream depths with hydraulically assisted bathymetry  
691 (HAB) models. *Geomorphology*, 72, pp. 320–339.

692 Fryer, J.G., 1983. A simple system for photogrammetric mapping in shallow water, *Photogrammetric Record*,  
693 11(62):203-208.

694 Giardino, C., Brando, V.E., Dekker, A.G., Strömbeck, N., Candiani, G., 2007. Assessment of water quality in Lake  
695 Garda (Italy) using Hyperion. *Remote Sensing of Environment*, 109 (2), pp. 183-195.

696 Gitelson, A.A. and Kondratyev, K.Y., 1991, Optical models of mesotrophic and eutrophic water bodies. *International  
697 Journal of Remote Sensing*, 12, pp. 373–385.

698 Gordon, H.R., 1990. Radiometric considerations for ocean color remote sensors. *Applied Optics*. 29, 3228–3236.

699 Haaland, D.M., and Thomas, E.V., 1988. Partial Least-Squares methods for spectral analyses. 1. Relation to other  
700 quantitative calibration methods and the extraction of qualitative information. *Analytical Chemistry*;60:1193–  
701 202.

702 Haenlein, M., Kaplan, A.M., 2004. A beginner's guide to partial least squares analysis. *Underst. Stat*, 3, 283–297.

703 Howley, T., Madden, M.G., O'Connell, M.L., Ryder, A.G., 2006. The effect of principal component analysis on  
704 machine learning accuracy with high-dimensional spectral data. *Knowledge-Based Systems*, 19(5), 363-370.

705 Hugue, F., Lapointe, M., Eaton, B.C., Lepoutre, A., 2016. Satellite-based remote sensing of running water habitats at  
706 large riverscape scales: Tools to analyze habitat heterogeneity for river ecosystem management.  
707 *Geomorphology*, 253, 353–369.

708 Jawak, S.D., and Luis, A.J., 2016. High-resolution multispectral satellite imagery for extracting bathymetric  
709 information of Antarctic shallow lakes ", *Proc. SPIE 9878, Remote Sensing of the Oceans and Inland Waters:  
710 Techniques, Applications, and Challenges*, 987819: doi:10.1117/12.2222769.

711 Jordan, D.C., Fonstad, M.A. 2005. Two-dimensional mapping of river bathymetry and power using aerial photography  
712 and GIS on the Brazos River, Texas. *Geocarto* 20(3): 1–8.

713 Kay, S., Hedley, J.D., and Lavender, S., 2009, Sun Glint Correction of High and Low Spatial Resolution Images of  
714 Aquatic Scenes: a Review of Methods for Visible and Near-Infrared Wavelengths, *Remote Sensing*, 1, 697-730.

715 Kinzel, P.J., Legleiter, C.J., and Nelson, J.M. 2013. Mapping river bathymetry with a small footprint green LiDAR:  
716 Applications and challenges. *Journal of the American Water Resources Association*, 49(1): 183-204.

717 Kirk, J.T.O., 1996. *Light & Photosynthesis in Aquatic Ecosystems*, 2nd ed.; Cambridge University Press: Cambridge,  
718 UK.

719 Lane, S.N., Widdison, P.E., Thomas, R.E., Ashworth, P.J., Best, J.L., Lunt, I.A., Sambrook Smith, G.H., Simpson,  
720 C.J., 2010. Quantification of braided river channel change using archival digital image analysis, *Earth Surface*  
721 *Processes and Landform*, 35(8), pp. 971–985.

722 Lee, Z.P., Carder, K.L., Mobley, C.D., Steward, R.G., Patch, J.S., 1998, Hyperspectral remote sensing for shallow  
723 waters, 1. A semi-analytical model. *Applied Optics*, 37, 6329–6338.

724 Lee, Z.P., Carder, K.L., Mobley, C.D., Steward, R.G., Patch, J.S., 1999. Hyperspectral remote sensing for shallow  
725 waters, 2. Deriving bottom depths and water properties by optimization. *Applied Optics*, 38, 3831–3843.

726 Legleiter, C.J., 2013. Mapping river depth from publicly available aerial images. *River Research and Applications*,  
727 29(6): 760-780.

728 Legleiter, C.J., and Overstreet, B.T. 2012. Mapping gravel-bed river bathymetry from space. *Journal of Geophysical*  
729 *Research - Earth Surface*, 117(F04024): doi: 10.1029/2012jf002539.

730 Legleiter, C.J., and Overstreet, B.T. 2014. Retrieving river attributes from remotely sensed data: An experimental  
731 evaluation based on field spectroscopy at the Outdoor Stream Lab. *River Research and Applications*, 30(6):  
732 671-684.

733 Legleiter, C.J., and Roberts, D.A., 2009. A forward image model for passive optical remote sensing of river  
734 bathymetry. *Remote Sensing of Environment*, 113 (5): 1025-1045.

735 Legleiter, C.J., Mobley, C.D., and Overstreet, B.T., 2017. A framework for modeling connections between hydraulics,  
736 water surface roughness, and surface reflectance in open channel flows. *Journal of Geophysical Research -*  
737 *Earth Surface*, 122(9): 1715-1741.

738 Legleiter, C.J., Overstreet, B.T., Glennie, C., Zhigang, P., Fernandez-Diaz, J., and Singhanian, A. 2016. Evaluating the  
739 capabilities of the CASI hyperspectral imaging system and Aquarius bathymetric LiDAR for measuring channel  
740 morphology in two distinct river environments. *Earth Surface Processes and Landforms*, 41(3): 344-363.

741 Legleiter, C.J., Roberts, D.A., and Lawrence, R.L. 2009. Spectrally based remote sensing of river bathymetry. *Earth*  
742 *Surface Processes & Landforms*, 34(8): 1039-1059.

743 Legleiter, C.J., Roberts, D.A., Marcus, W.A., Fonstad, M.A., 2004. Passive optical remote sensing of river channel  
744 morphology and in-stream habitat: Physical basis and feasibility. *Remote Sensing of Environment*, 93, 493-510.

745 Legleiter, C.J., Stegman, T.K., and Overstreet, B.T. 2016. Spectrally based mapping of riverbed composition.  
746 *Geomorphology*, 264: 61-79.

747 Lesser, M.P., Mobley, C.D., 2007, Bathymetry, water optical properties, and benthic classification of coral reefs using  
748 hyperspectral remote sensing imagery. *Coral Reefs*, 26, 819–829.

749 Li, X., Zhang, Y., Bao, Y., Luo, J., Jin, X., Xu, X., Song, X., and Yang G., 2014. Exploring the Best Hyperspectral  
750 Features for LAI Estimation Using Partial Least Squares Regression. *Remote Sensing*, 6, pp. 6221-6241.

751 Louchard, E.M., Reid, R.P., Stephens, F.C., Davis, C.O., Leathers, R.A., Valerie, D.T., 2003. Optical remote sensing  
752 of benthic habitats and bathymetry in coastal environments at Lee Stocking Island, Bahamas: A comparative  
753 spectral classification approach. *Limnology and Oceanography*, 48 (2003), pp. 511–521.

754 Lyzenga, D.R., 1978. Passive remote sensing techniques for mapping water depth and bottom features. *Applied Optics*,  
755 17, 379–383.

756 Lyzenga, D.R., 1981, Remote sensing of bottom reflectance and water attenuation parameters in shallow water using  
757 aircraft and Landsat data, *International Journal of Remote Sensing*, 2:1, 71-82.

758 Lyzenga, D.R., 1985. Shallow-Water Bathymetry Using Combined Lidar and Passive Multispectral Scanner Data.  
759 *International Journal of Remote Sensing*, 6, 115-125.

760 Lyzenga, D.R., Malinas, N.P. and Tanis, F.J., 2006. Multispectral bathymetry using a simple physically based  
761 algorithm, *IEEE Transactions on Geoscience and Remote Sensing*, 44(8), 2251-2259.

762 Marcus, W. A., and Fonstad, M.A., 2008. Optical remote mapping of rivers at sub-meter resolutions and watershed  
763 extents, *Earth Surface Processes & Landforms*, 33(1), 4–24.

764 Marcus, W. A., and Fonstad, M.A., 2010. Remote sensing of rivers: The emergence of a subdiscipline in the river  
765 sciences, *Earth Surface Processes & Landforms*, 35(15), 1867–1872.

766 Markovitch, S., and Rosenstein, D., 2002, Feature Generation Using General Constructor Functions, *Machine*  
767 *Learning*, 49, 59–98.

768 Martens, H.A., Dardenne, P., 1998. Validation and verification of regression in small data sets, *Chemometrics and*  
769 *Intelligent Laboratory Systems*, 44, pp. 99–121.

770 MATLAB, 2018, MATLAB User's Guide. The Math Works, Inc., Natick, MA.

771 Mobley, C.D., 1994. Light and water: Radiative transfer in natural waters. Academic: San Diego, USA.

772 Mobley, C.D., and Sundman, L.K., 2008. Hydrolight 5, Ecolight5 User Guide, Sequoia Scientific, Inc., Bellevue.

773 Montgomery, D.R., Buffington, J.M., Smith, R.D., Schmidt, K.M., and Pess, G., 1995. Pool spacing in forest channels.  
774 *Water Resources Research*, 31(4), 1097-1105.

775 Mouw, C.B., Greb, S., Aurin, D.A., DiGiacomo, P.M., Lee, Z., Twardowski, M., Binding, C., Hu, C., Ma, R., Moore,  
776 T., Moses, W., Craig, S.E., 2015. Aquatic color radiometry remote sensing of coastal and inland waters:  
777 challenges and recommendations for future satellite missions. *Remote Sens. Environ.* 160, 15–30, <http://dx.doi.org/10.1016/j.rse.2015.02.001>.

778

779 Mumby, P. J., and Edwards, A. J., 2000. Water column correction approaches. In E. P. Green, P. J. Mumby, A. J.  
780 Edwards, & C. D. Clark (Eds.), *Remote sensing handbook for tropical coastal management*. Paris: Unesco. 316  
781 pp.

782 Niroumand-Jadidi, M. and Vitti, A., 2016, Optimal Band Ratio Analysis of WorldView-3 Imagery for Bathymetry of  
783 Shallow Rivers (case Study: Sarca River, Italy), *ISPRS - International Archives of the Photogrammetry, Remote*  
784 *Sensing and Spatial Information Sciences*, Volume XLI-B8, 2016, pp. 361-364.

785 Niroumand-Jadidi, M. and Vitti, A., 2017b. Grain Size Mapping in Shallow Rivers Using Spectral Information: A  
786 Lab Spectroradiometry Perspective, *Proc. SPIE 10422, Remote Sensing of the Ocean, Sea Ice, Coastal Waters,*  
787 *and Large Water Regions 2017*, 104220B.

788 Niroumand-Jadidi, M., and Vitti, A., 2017a. Reconstruction of river boundaries at sub-pixel resolution: Estimation  
789 and spatial allocation of water fractions. *ISPRS International Journal of Geo-Information*, 6, 383.

790 Overstreet, B.T., and Legleiter, C.J. 2017. Removing sun glint from optical remote sensing images of shallow rivers.  
791 *Earth Surf Processes & Landforms*, 42(2): 318-333.

792 Pacifici, F., 2016. Atmospheric Compensation in Satellite Imagery. US Patent 9396528B2.

793 Pacifici, F., Longbotham, N., and Emery, W. J., 2014. The Importance of Physical Quantities for the Analysis of  
794 Multitemporal and Multiangular Optical Very High Spatial Resolution Images, *IEEE Transactions on*  
795 *Geoscience and Remote Sensing*, 52(10),6241-6256.

796 Pahlevan, N., Roger, J.-C., Ahmad, Z., 2017. Revisiting short-wave-infrared (SWIR) bands for atmospheric correction  
797 in coastal waters. *Optics Express*, 25 (2017), pp. 6015-6035.

798 Philpot, W. D. 1989. Bathymetric mapping with passive multispectral imagery. *Applied Optics*, 28: 1569–1578.

799 Qian, Y., Ye, M., and Zhou, J., 2012, Hyperspectral Image Classification Based on Structured Sparse Logistic  
800 Regression and Three-Dimensional Wavelet Texture Features, *IEEE Transactions on Geoscience and Remote*  
801 *Sensing*, VOL. 51, NO. 4, 2276-2291.

802 Reunanen, J., 2003. Overfitting in Making Comparisons Between Variable Selection Methods. *Journal of Machine*  
803 *Learning Research*, 3, 1371-1382.

804 Shintani C., and Fonstad, M.A., 2017. Comparing remote-sensing techniques collecting bathymetric data from a  
805 gravel-bed river, *International Journal of Remote Sensing*, DOI: 10.1080/01431161.2017.1280636.

806 Stumpf, R. P., Holderied, K., and Sinclair, M., 2003. Determination of water depth with high-resolution satellite  
807 imagery over variable bottom types. *Limnology and Oceanography*, 48, pp. 547–556.

808 Walther, S.C., Marcus, W.A., Fonstad, M.A., 2011. Evaluation of high resolution, true colour, aerial imagery for  
809 mapping bathymetry in a clear water river without ground-based depth measurements. *International Journal of*  
810 *Remote Sensing*, 32 (15), pp. 4343–4363.

811 Westaway, R.M., Lane, S.N., and Hicks, D.M., 2001. Airborne remote sensing of clear water, shallow, gravel-bed  
812 rivers using digital photogrammetry and image analysis. *Photogrammetric Engineering and Remote Sensing*,  
813 67: pp. 1271–1281.

814 Winterbottom, S. J., and Gilvear, D. J., 1997. Quantification of channel bed morphology in gravel-bed rivers using  
815 airborne multispectral imagery and aerial photography, *Regulated Rivers: Research & Management*, 13(6),  
816 489–499.

- 817 Wold, S., Sjostrom, M., and Eriksson, L., 2001. PLS-regression: a basic tool of chemometrics, *Chemometrics and*  
818 *Intelligent Laboratory Systems*, 58(2), 109–130.
- 819 Woodget, A.S., Carbonneau, P.E., Visser, F., and Maddock, I.P., 2015. Quantifying submerged fluvial topography  
820 using hyperspatial resolution UAS imagery and structure from motion photogrammetry. *Earth Surface*  
821 *Processes and Landforms*, 40: 47–64.